

1 **Spatial variation in shallow slow earthquake activity in Hyuga-nada, southwest Japan**

2
3 Satoru Baba^{1,2}, Shunsuke Takemura¹, Kazushige Obara¹, Akiko Takeo¹, Yusuke Yamashita³, and
4 Masanao Shinohara¹

5
6 1. Earthquake Research Institute, the University of Tokyo, 1-1-1, Yayoi, Bunkyo-ku, Tokyo,
7 113-0032, Japan

8 2. Now at Japan Agency for Marine-Earth Science and Technology, 2-15, Natsushima-cho,
9 Yokosuka, Kanagawa, 237-0061, Japan

10 3. Miyazaki Observatory, Disaster Prevention Research Institute, Kyoto University, 3884 Kaeda,
11 Miyazaki, Miyazaki, 889-2161, Japan

12
13 **Abbreviated title:** Spatial variation in slow earthquakes in Hyuga-nada

14
15 **Corresponding author:** Satoru Baba

16 E-mail: babasatoru@jamstec.go.jp

17 Phone: +81-46-867-9342

20 **Summary**

21 Hyuga-nada, off the Pacific coast of Kyushu along the Nankai Trough in southwest
22 Japan, is one of the most active slow earthquake regions around Japan. We estimated the energies
23 of shallow tremors and moments of shallow very low frequency earthquakes (VLFs) in Hyuga-
24 nada using data from a permanent onshore broadband network and temporary ocean bottom
25 seismometer observations. The energies and moments of these slow earthquakes have a similar
26 along-strike variation and are generally larger south of the subducted Kyushu-Palau Ridge than
27 near the top of the ridge. This spatial variation is also related to the characteristics of slow
28 earthquake migration. The along-strike migration speed was faster at initiation in the south, where
29 the moments of slow earthquakes are larger. After migration entered the subducted Kyushu-Palau
30 Ridge, its speed is decelerated with a parabolic pattern and their moments became smaller.
31 Assuming a constant patch size of slow earthquakes, we estimated that the stress drop of VLFs
32 in the south of the subducted ridge was approximately three times larger than that near the top of
33 the subducted ridge. According to our observations and a physical model, this stress drop
34 difference between adjacent regions may cause parabolic migration. We also estimated the scaled
35 energy of slow earthquakes from the ratio of the seismic energy rates of tremors to the seismic
36 moment rates of accompanying VLFs. The spatial variation in scaled energy is not identified
37 inside the Hyuga-nada. Since the range of scaled energy is similar between Areas A and B, the
38 apparent stress may be similar if the rigidity is the same. The dominant range of scaled energy of
39 slow earthquakes in Hyuga-nada is $10^{-11.5}$ – $10^{-8.5}$. In addition to having similar or one order smaller
40 values compared to other slow earthquake regions, the range of scaled energy in Hyuga-nada is
41 broader. This broader range suggests wide range of characteristic time and various spectral
42 features of slow earthquakes in Hyuga-nada. Based on a Brownian slow earthquake model, the
43 wide range of characteristic time in this area suggests width variations of slow earthquake source
44 area.

45

46 **Keywords:** Subduction zone processes, Seismicity and tectonics, Earthquake source observations,
47 Japan

48

49

50 **1. Introduction**

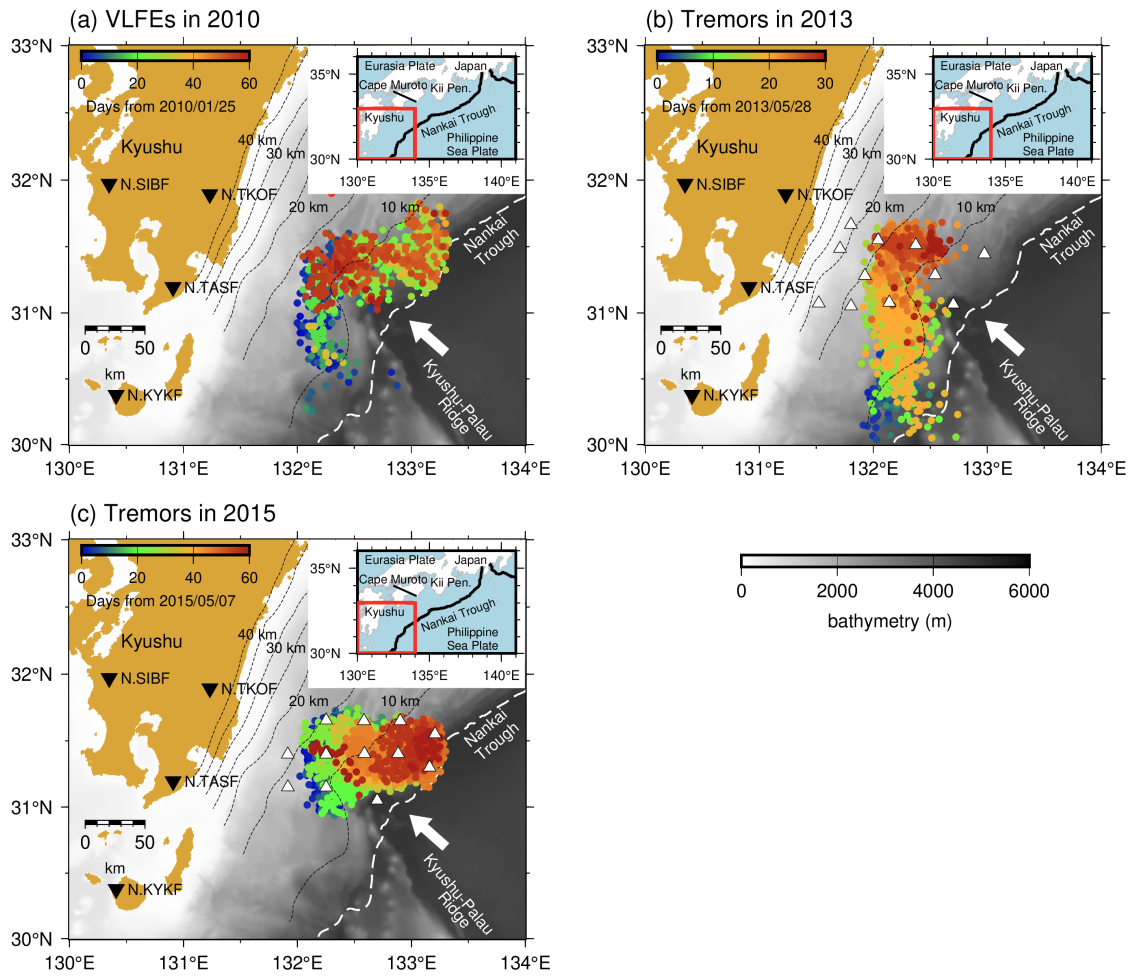
51 After the discovery of tectonic low frequency tremors by Obara (2002), slow
52 earthquakes, which are fault slips with longer characteristic durations than regular earthquakes
53 with the same seismic moment (Ide *et al.* 2007), were mainly detected around seismogenic zones
54 on plate boundaries of subduction zones or strike slip regimes in the world. Seismic slow
55 earthquakes are classified into tremors and low frequency earthquakes (e.g., Shelly *et al.* 2006)
56 observed in a frequency range of 2–8 Hz, and very low frequency earthquakes (VLFs) observed
57 in a frequency range of 0.02–0.05 Hz (e.g., Obara & Ito 2005). Slow slip events (SSEs) are
58 geodetically observed as crustal deformations, with duration ranging from several days to several
59 years (e.g., Dragert *et al.* 2001; Hirose *et al.* 1999). The focal mechanisms of slow earthquakes in
60 subduction zones are thrust-type and consistent with those of megathrust earthquakes along plate
61 boundaries. In addition, slow earthquake activity can reflect the stress conditions on the plate
62 boundary around the slow earthquake regions (e.g., Obara & Kato 2016). Recent studies have
63 revealed that slow earthquakes can potentially trigger megathrust earthquakes (e.g., Kato *et al.*
64 2012; Vaca *et al.* 2018). Thus, studies of slow earthquakes are important for understanding the
65 slip behaviours on the plate boundary and the occurrence mechanism of megathrust earthquakes.

66 Around the Japanese islands, slow earthquakes occur in shallower and deeper extensions
67 of the seismogenic zone in southwest Japan along the Nankai Trough and in the offshore region
68 of northeastern Japan along the Japan Trench. In Hyuga-nada, off the Pacific coast of Kyushu,
69 VLFs are the most active around Japan (Baba *et al.* 2020). In this area, Asano *et al.* (2015)
70 reported the migration of shallow VLFs, which can be considered as a proxy for rupture
71 propagation of an SSE (e.g., Bartlow *et al.* 2011; Ito *et al.* 2007), in 2010 (Fig. 1a). VLFs first
72 migrated from 30.5° N to 31.5° N along the strike direction and changed to along-dip migration
73 at the subducted Kyushu-Palau Ridge, which is subducting at the Nankai Trough. Although
74 VLFs are observed by onshore stations owing to the effective propagation of surface waves
75 along shallower low velocity structures, it is difficult to identify weak signals of shallow tremors
76 in Hyuga-nada using permanent onshore stations. Yamashita *et al.* (2015) and Yamashita *et al.*
77 (2021) detected shallow tremors and reported their migrations in Hyuga-nada utilizing temporary
78 ocean bottom seismometers (OBSs) in 2013 and 2015, respectively (Fig. 1b and c). In 2013,
79 tremors migrated twice from 30.3° N to 31.7° N. In 2015, tremors migrated from west to east,
80 north of 31° N and extended near the trench axis (Yamashita *et al.* 2021). The shallow tremors in
81 Hyuga-nada were temporally correlated with shallow VLFs (Fig. 2). The spatial distributions of
82 tremors in both 2013 and 2015 were contained by those of VLFs in 2010. Temporary OBS
83 observations also revealed a high-resolution distribution of VLFs. Tonegawa *et al.* (2020)
84 suggested that the depths of shallow VLFs near the subducted Kyushu-Palau Ridge are
85 approximately 5 km different from the surrounding area.

86 The tectonic regime in Hyuga-nada is very characteristic; the Kyushu-Palau Ridge is
87 subducting and the trench axis bends around the region where the ridge subducts (Fig. 1). In
88 addition, repeating earthquakes representing quasi-static slips on the plate boundary (e.g., Nadeau
89 & McEvilly 1999; Uchida et al. 2003) occur in the downdip of shallow slow earthquakes (e.g.,
90 Igarashi, 2020; Yamashita et al., 2012). Tectonic conditions can affect the source parameters, such
91 as the moment rate, of slow earthquakes (Baba et al. 2020; Takemura et al. 2022b). To investigate
92 the spatial relationships between slow earthquake activity and tectonic conditions in Hyuga-nada
93 in this study, we quantitatively estimated the spatial variation in the source characteristics of slow
94 earthquakes at high spatial resolution using onshore and offshore data.

95 As the quantitative indicators of source characteristics, we focus on the energy rate
96 functions of tremors, moment rate functions of VLFs, and the scaled energy. Recently, slow
97 earthquake signals have been also detected in the microseism frequency band between tremors
98 and VLFs (Kaneko et al. 2018; Masuda et al. 2020; Yamashita et al. 2021); therefore, slow
99 earthquakes are assumed to be broadband phenomena (Ide & Maury, 2018). Ide et al. (2008)
100 demonstrated the seismic energy rates of slow earthquakes in 2–8 Hz are proportional to the
101 seismic moment rates and evaluated the scaled energy of slow earthquakes by the ratio between
102 tremor energy rate and the accompanying VLFE moment rate. Scaled energy has been used for
103 the purpose of comparing dynamic characteristics of seismic events (Kanamori & Rivera 2006). If
104 the rupture process of seismic events is self-similar, the scaled energy is constant. Previous studies
105 demonstrated that scaled energy of slow earthquakes is 10^{-10} – 10^{-8} and 4–5 orders smaller than that
106 of regular earthquakes (e.g., Ide et al. 2008). Yabe et al. (2019) and Yabe et al. (2021) estimated
107 the scaled energy of shallow slow earthquakes along the Nankai Trough and along the Japan
108 Trench, respectively, and suggested the relationship between scaled energy distribution and
109 geological condition. To investigate the characteristics of broadband slow earthquakes as well as
110 the spatial relationships between slow earthquake activity and tectonic conditions, we evaluated
111 the energy rate functions of tremors, the moment rate functions of VLFs, and the scaled energy
112 of the slow earthquakes in Hyuga-nada at a high spatial resolution using onshore and offshore
113 data.

114

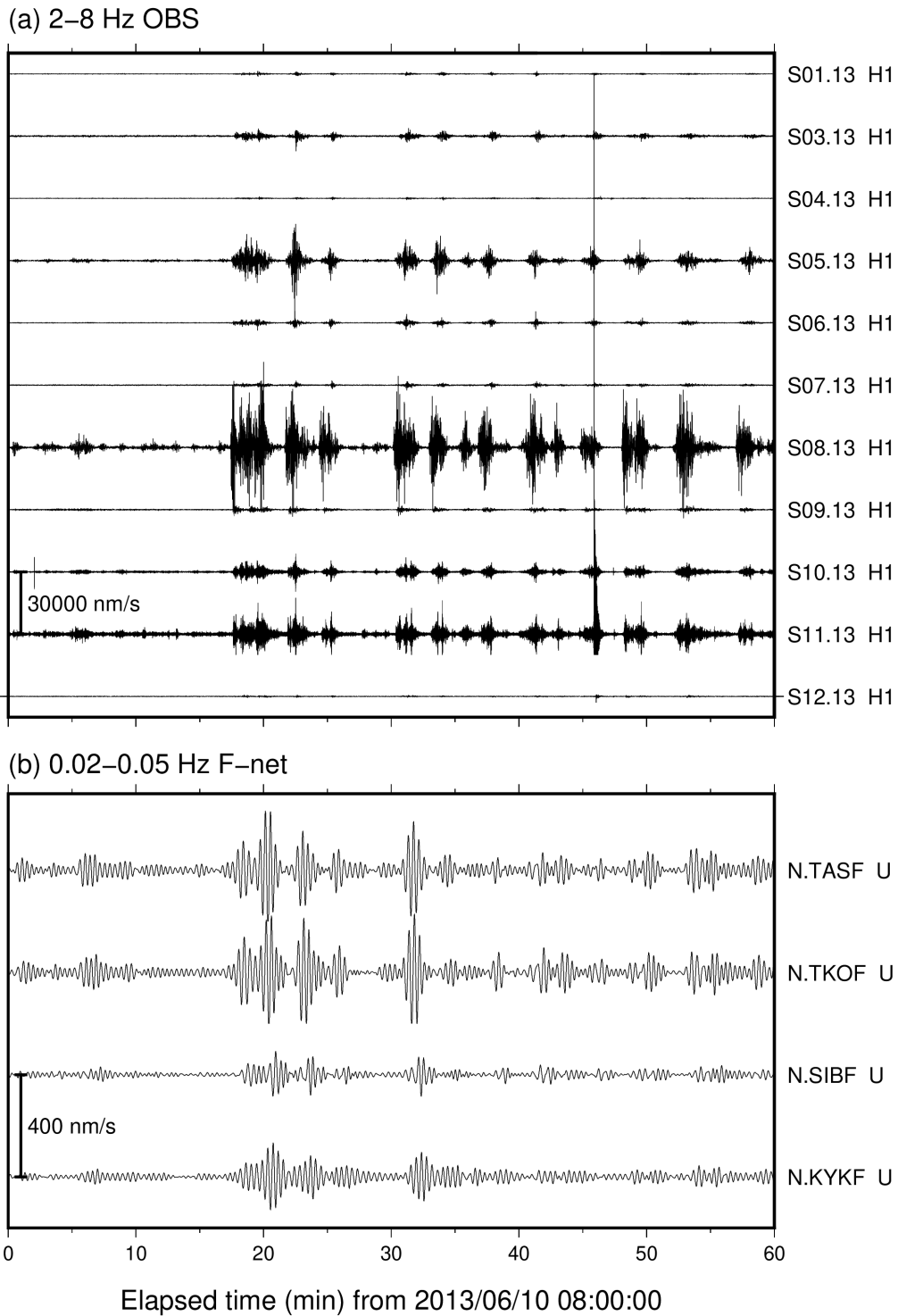


115

116

117 **Figure 1.** Slow earthquake activity in Hyuga-nada. Coloured dots are epicentres of (a) shallow
 118 VLFs in 2010 detected by Asano et al. (2015), (b) shallow tremors in 2013 detected by
 119 Yamashita et al. (2015), and (c) shallow tremors in 2015 detected by Yamashita et al. (2021). The
 120 colours of dots correspond to days from the first activity for each tremor episode. White triangles
 121 represent the locations of the OBSs utilized in the shallow tremor analysis. Inverted triangles
 122 exhibit the locations of the F-net stations utilized in the shallow VLFE analysis. White arrows
 123 indicate the direction of the motion of the Philippine Sea Plate relative to the Eurasia Plate
 124 (NUVEL-1A; DeMets et al., 1994). White dashed lines represent the trench axis. Background
 125 grey scale denotes the bathymetry (ETOPO1; Amante & Eakins 2009). Dashed contours indicate
 126 the isodepth at the top of the Philippine Sea plate in intervals of 5 km (Nakanishi *et al.* 2018).
 127 Black lines in the inset represent the boundaries between the plates.

128



129

130

131 **Figure 2.** Example of one-hour records for (a) shallow tremors in a frequency range of 2–8 Hz at

132 OBSs and (b) shallow VLFES in a frequency range of 0.02–0.05 Hz at F-net stations.

133

134 **2. Data and Method**

135 **2.1. Estimation of energy rate functions of tremors**

136 For the analysis of tremors, we evaluated the energy rate functions of tremors located
 137 by Yamashita et al. (2015; 2021). We used 360 s broadband (NK1508 and NK1510 in 2015), 1
 138 Hz (S06.13, S09.13 in 2013 and others in 2015) and 4.5 Hz (others in 2013) short-period OBS
 139 records of temporary seismological observations in Hyuga-nada. 11 and 12 stations were
 140 incorporated from April 17 to July 4, 2013 (Yamashita et al. 2015) and from January 1, 2015 to
 141 January 1, 2016 (Yamashita et al. 2021), respectively. The sampling rates were 200 Hz (S05.13,
 142 S06.13, S08.13, and S09.13 in 2013 and all OBSs in 2015) or 128 Hz (other OBSs in 2013).
 143 Analog seismic signals were digitized using a 16-, 20-, or 24-bit A/D converter. After instrumental
 144 responses were removed, a bandpass filter was applied in a frequency range of 2–8 Hz, and the
 145 vertical and horizontal components of the root-mean-square (RMS) velocity envelopes with a
 146 smoothing time window of 5 s were calculated. The envelopes were resampled at one sample per
 147 second. Examples of envelope waveforms of a tremor obtained by the RMS of the sums squared
 148 seismograms of two horizontal components are displayed in Fig. 3. Since OBSs are often installed
 149 on soft sediments and amplitudes of seismic waves are more amplified compared to onshore
 150 stations. We, therefore, selected a permanent onshore station N.TASF from the F-net broadband
 151 seismograph network (Aoi *et al.* 2020) as a reference station, because F-net stations are installed
 152 at inland outcrop rock sites (Aoi et al., 2020) and the site amplification factors between F-net
 153 stations are very similar (Takemoto *et al.* 2012).

154 We estimated the site amplification factors of the vertical and horizontal components
 155 at each OBS relative to N.TASF, at 2–8 Hz and the quality factor of the *S*-wave attenuation (Q)
 156 by utilizing the information of the maximum *S*-wave amplitudes of intraslab regular earthquakes
 157 following the method of Yabe et al. (2019). The maximum *S*-wave amplitude of the i -th
 158 earthquake at the j -th station (A_{ij}) is expressed by the following relationship:

159
$$\ln(A_{ij}) = \ln(S_i) - \ln(\sqrt{4\pi}L_{ij}) - \frac{\pi f_c Q^{-1}}{V_s} L_{ij} + \ln(C_j) \quad (1)$$

160 where S_i is the size of the i -th seismic source, L_{ij} is the distance between the hypocentre of the i -
 161 th earthquake and the j -th station, f_c represents the central frequency (5 Hz in this study), V_s is the
 162 *S*-wave velocity (assuming 3.5 km/s in this study), and C_j is the site amplification factor. Q^{-1}
 163 represents apparent *S*-wave attenuation, including intrinsic and scattering attenuations. The
 164 attenuation by geometrical spreading corresponds to the second term of the right-hand side of the
 165 equation (1). We measured the maximum *S*-wave amplitudes of regular earthquakes more than 5
 166 km deeper than the plate boundary of the Japan Integrated Velocity Structure Model (JIVSM;
 167 Koketsu et al. 2012) with magnitudes larger than 2.5 listed in the regular earthquake catalogue of
 168 the Japan Meteorological Agency (Fig. S1). We defined the maximum envelope amplitude of the

169 time window from 2 s before to 50 s after the arrival time at each OBS as the maximum S -wave
 170 amplitude. To estimate the site amplification factor of j -th station relative to a reference station
 171 (j_0), taking the difference of equation (1) for i -th event at j -th and the reference station:

$$172 \quad \ln\left(\frac{A_{ij}}{A_{ij_0}}\right) + \ln\left(\frac{L_{ij}}{L_{ij_0}}\right) = -\frac{\pi f_c Q^{-1}}{V_S}(L_{ij} - L_{ij_0}) + \ln\left(\frac{C_j}{C_{j_0}}\right). \quad (2)$$

173 The site amplification factor relative to N.TASF and Q^{-1} at each OBS was estimated by solving
 174 Equation (2) using the least-squares method. Following Yabe et al. (2019), we set the site
 175 amplification factor at the reference station N.TASF as 2 to consider the free-surface effect. In the
 176 following procedures, we utilized the RMS of the sums of the squared three-component
 177 seismograms with a smoothing time window of 5 s after site correction by implementing the site
 178 amplification factors displayed in Fig. 4. After correcting the site amplification factors, the
 179 amplitudes were normalized by the site conditions at the reference onshore station, N.TASF. We
 180 also evaluated the average of Q^{-1} solved at each OBS in Equation (2) as $(3.4415 \pm 0.9585) \times 10^{-3}$.
 181 We adopted this value to estimate the energy rate functions of the tremors.

182 We calculated the energy rate functions of the tremors by implementing the site
 183 amplification factors and Q^{-1} estimated by the above procedures. The energy rate function of a
 184 tremor ($E_j(t)$), estimated from the amplitudes of the j -th station, was calculated using the following
 185 equation:

$$186 \quad E_j(t) = 2\pi V_S r_j^2 \rho A''_j(t + t_j) \exp(2\pi f_c Q^{-1} t_j) \quad (3)$$

187 where, $A''_j(t)$ is the amplitude of envelopes after the site-correction at the j -th station, r_j is the
 188 hypocentral distance from the tremor source to the j -th station, t_j is the travel time from the tremor
 189 source to the j -th station, and ρ is the density (assuming $2,700 \text{ kg/m}^3$ in this study). The epicentral
 190 locations of the tremors were set at those located by Yamashita et al. (2015; 2021). The depth of
 191 the tremors was set at the plate boundary of the JIVSM (Koketsu et al. 2012). To calculate the
 192 energy rate function, the time windows were set at 240 s, which started 60 s before the time
 193 window of the tremors set by Yamashita et al. (2015; 2021). We stacked the energy rate functions
 194 of a tremor for each station and estimated the average energy rate function $E_{ave}(t)$ divided by the
 195 number of stations used. We calculated the cross-correlation coefficients (CCs) of the energy rate
 196 functions of all station pairs in Fig. 4 and further utilized the stations whose CCs exceeded 0.6
 197 with at least one other station when stacking the energy rate functions.

198 The seismic energy W of a tremor is calculated by integrating $E_{ave}(t)$ in the time range
 199 t_1-t_2 :

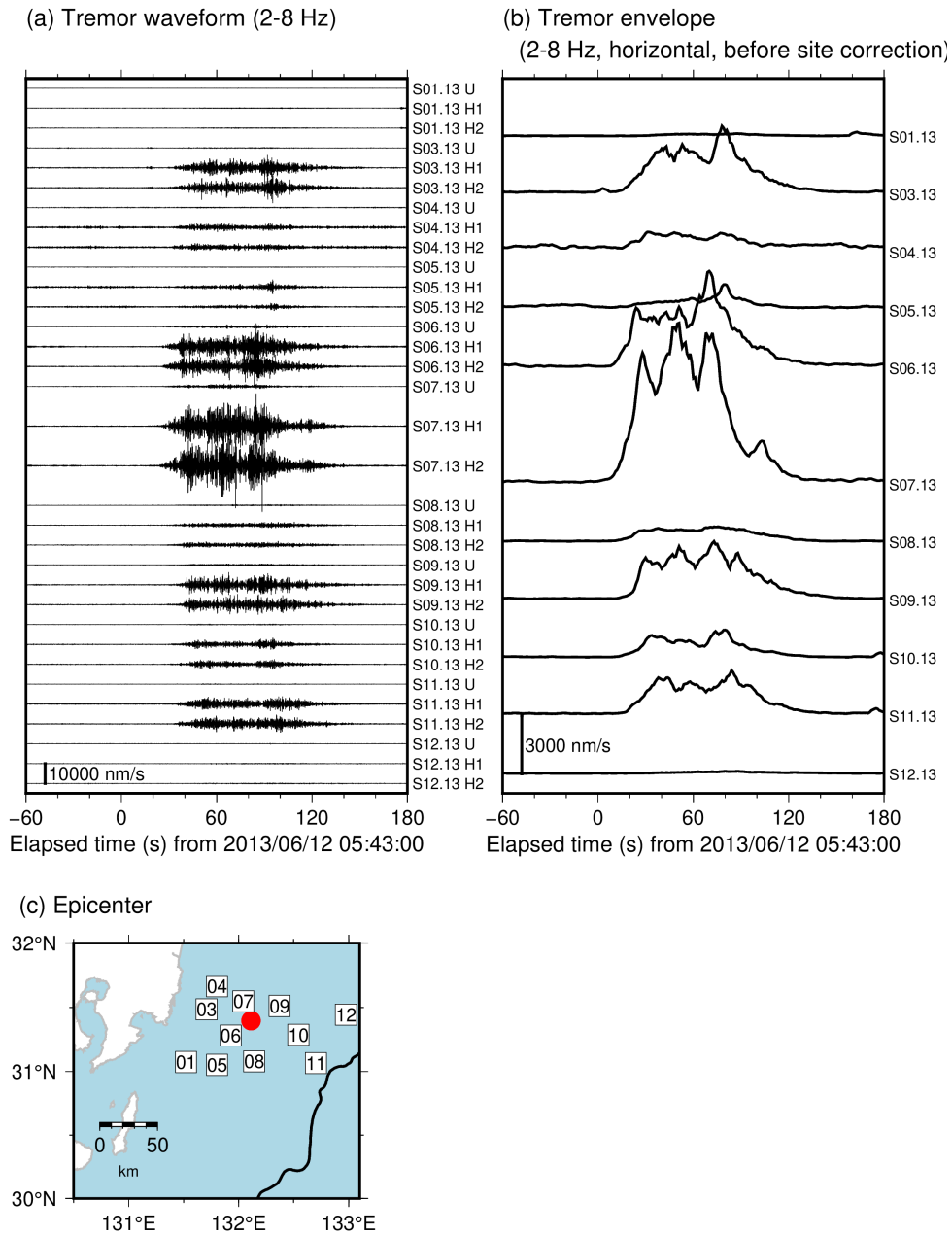
$$200 \quad W = \int_{t_1}^{t_2} E_{ave}(t) dt. \quad (4)$$

201 The integration range is the period when the values of $E_{ave}(t)$ exceed 20% of the maximum
 202 value of $E_{ave}(t)$ (red line in the stacked energy rate function of Fig. 5). The duration of a tremor

203 was defined as $t_2 - t_1$. The seismic energy rate of the tremor was estimated by dividing the
204 seismic energy by the duration. To evaluate the uncertainty of estimated energies, we calculated
205 the standard deviation of the logarithm of energies estimated from each OBS data. The uncertainty
206 of tremor energies is 0.5–1 order (Fig. S3a).

207 To validate the method of seismic energy estimation, we estimated seismic energies of
208 regular earthquakes in the 2015–2016 observation by using the equations (3) and (4) (Fig. S4).
209 The earthquakes in the area of 131.0°E–133.5°E and 30.0–32.0°N with moment magnitudes larger
210 than 4 by moment tensor analysis by F-net site
211 (<https://www.fnet.bosai.go.jp/event/search.php?LANG=en>) were selected. In previous studies,
212 scaled energies of regular earthquakes evaluated by the ratio of seismic energy to seismic moment
213 are estimated to be approximately 3×10^{-5} (e.g., Ide & Beroza 2001). The scaled energies of most
214 regular earthquakes shown in Fig. S4a are in the range of 10^{-5} – 10^{-4} (Fig. S4b). It indicates that
215 this method can estimate seismic energies on an order scale.

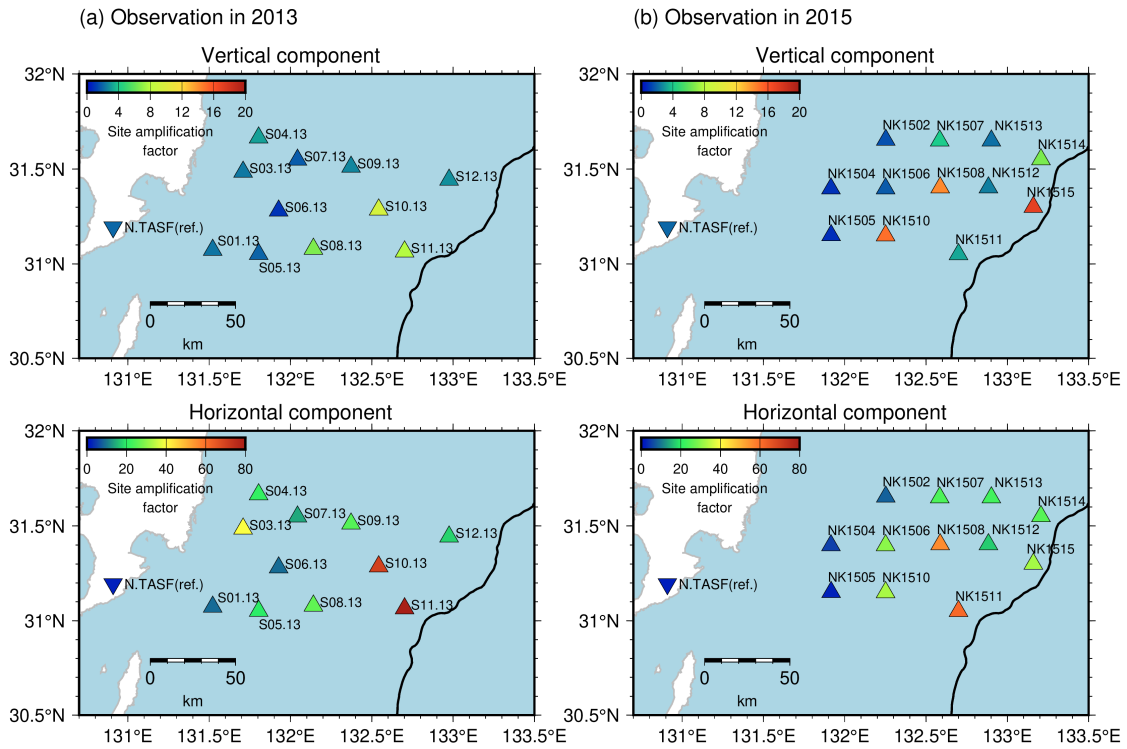
216



217

218

219 **Figure 3.** Example of (a) waveforms of a tremor in a frequency range of 2–8 Hz, and (b) envelopes
 220 obtained by the root-mean-square of sums squared seismograms of two horizontal components.
 221 Waveforms are displayed from 05:43:00 (JST, UTC+9), June 12, 2013. (c) Red circle depicts the
 222 epicentre of the tremor as displayed in in Fig. 3a and b. Black line represents the trench axis.
 223 Squares indicate the locations of OBSs.



224

225

226

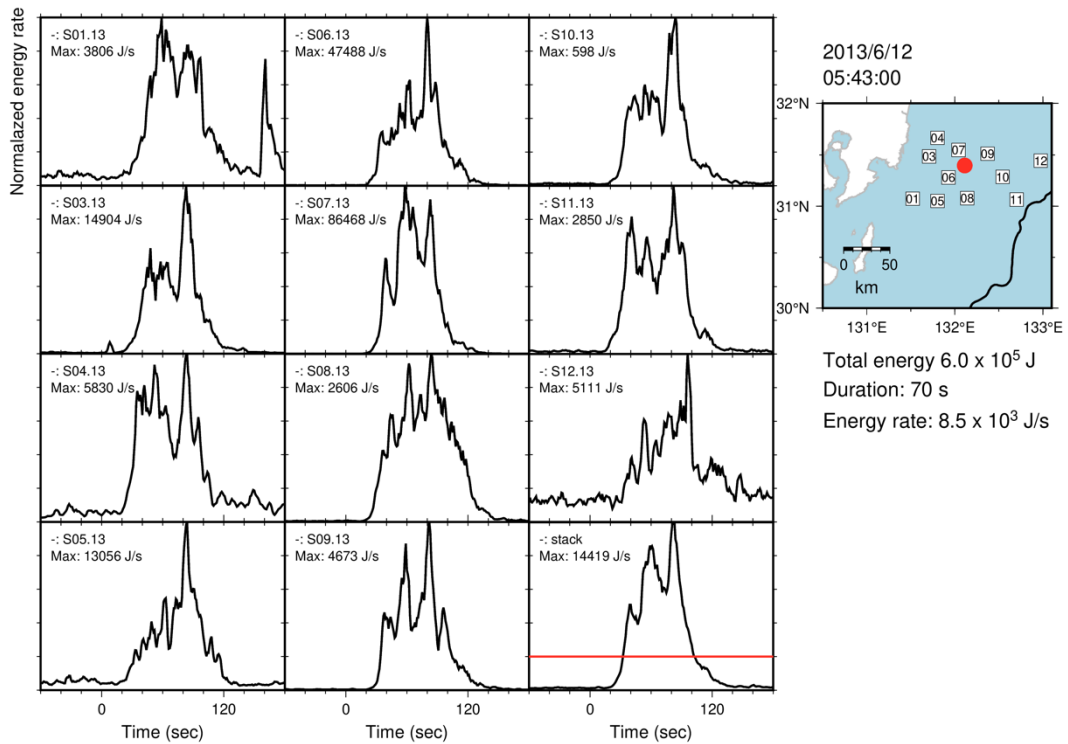
227

228

229

230

Figure 4. Site amplification factors at each OBS. Triangles represent the locations of OBSs. Inverted triangle indicates the location of the reference station, N.TASF. Black line is the same as displayed in Fig. 3. Estimation error of site amplification factors is shown in Fig. S2. Site amplification factor at N.TASF is set as 2.0.



231

232

233 **Figure 5.** Temporal changes of energy rate functions of a tremor estimated at each OBS along

234 with its stacked energy rate function. Red line of the stacked energy rate function indicates the

235 threshold, which is set as 20% of the maximum value of the energy rate function. Red circle,

236 squares and black line are the same as displayed in Fig. 3.

237

238 **2.2. Estimation of moments of VLFES**

239 We estimated the source durations and seismic moments of VLFES temporally
240 corresponding to the tremors in 2013 and 2015 detected by Yamashita et al. (2015; 2021) by
241 comparing observed and synthetic waveforms following the procedure of Yabe et al. (2021) and
242 Baba et al. (2021). We additionally estimated the source durations and seismic moments of VLFES
243 in 2010 detected by Asano et al. (2015) using the same method. As long-period VLFES signals are
244 difficult to recognize in short-period OBS records, we utilized continuous seismograms at onshore
245 broadband F-net stations for estimation. Before the analysis, we removed the instrumental
246 responses, resampled at one sample per second, and applied a bandpass filter in a frequency range
247 of 0.02–0.05 Hz to enhance the VLFES signals.

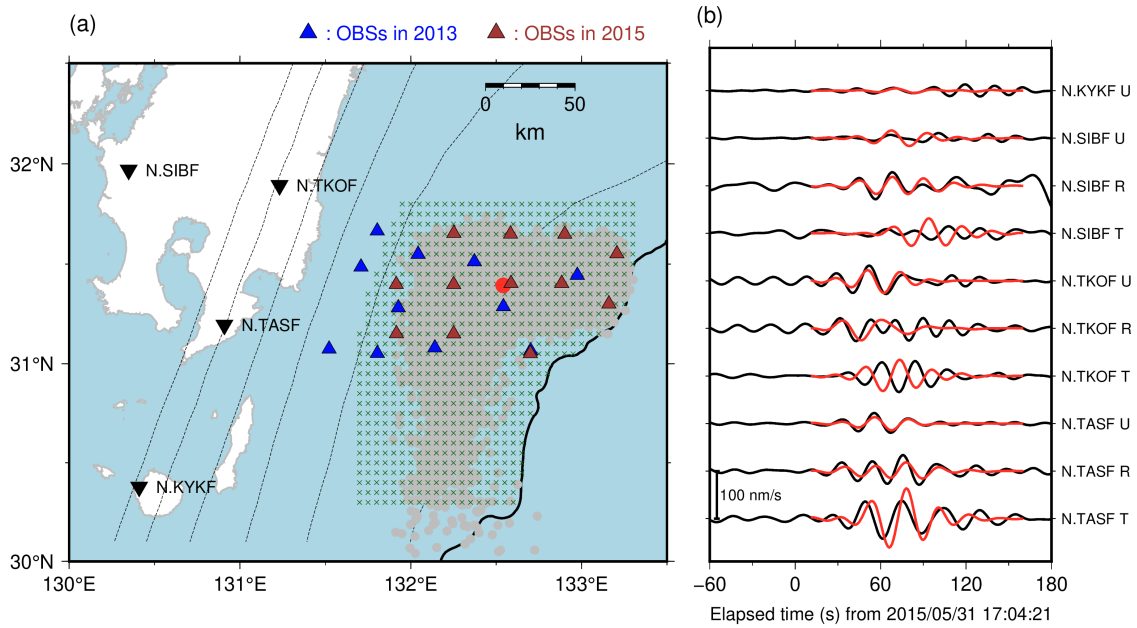
248 To reduce the computational costs of calculating Green's functions, reciprocal
249 calculations were conducted using OpenSWPC (Maeda *et al.* 2017). We set source grids at an
250 interval of 0.05° on the JIVSM plate boundary model of the area where tremors were detected
251 (Fig. 6a). The hypocentre of each VLFES was assumed to be at the nearest grid from the hypocentre
252 of the tremor located by Yamashita et al. (2015; 2021) or at the hypocentre of VLFES located by
253 Asano et al. (2015). JIVSM was implemented to calculate Green's functions. The minimum S-
254 wave velocity in the elastic volume was set as 1.5 km/s. The model includes topography
255 (ETOPO1; Amante & Eakins 2009), air, and seawater layers. The default values of OpenSWPC
256 were used for the density, seismic velocities, and quality factors in seawater and air. The model
257 volume was discretized using a uniform grid of 0.2 km. The focal mechanisms were assumed to
258 be consistent with the geometry of the plate boundary model of JIVSM and the plate convergence
259 direction of the plate motion model NUVEL-1A (DeMets *et al.* 1994). By combining the assumed
260 focal mechanisms and Green's functions, we prepared a series of synthetic velocity seismograms
261 with triangular functions and source durations of 10–50 s (e.g., Takemura et al., 2019).

262 We calculated the station- and component-averaged CCs between the synthetic and
263 observed waveforms. The time window of synthetic waveform is 150 s from the assumed origin
264 time of a VLFES. The origin time was searched for in the range from 30 s before to 30 s after the
265 start time of the duration range of each tremor located by Yamashita et al. (2015; 2021) and the
266 origin time of each VLFES located by Asano et al. (2015). The combination of source duration and
267 origin time, with the highest average CC in the grid search, was adopted. For tremor episodes in
268 2013 and 2015, if the highest averaged CC is larger than 0.3, we regard that a VLFES occurs
269 temporally corresponding to the tremor. The difference of origin times between a VLFES and the
270 corresponding tremor is in the range of ± 20 s. For VLFES episode in 2010, events with average
271 CCs smaller than 0.3 were discarded. We calculated the relative amplitudes by minimizing the
272 variance reduction between simulated and observed waveforms (Baba et al. 2021; Yabe et al.
273 2021), and further estimated the seismic moments of VLFES using the estimated relative

274 amplitudes. The moment, duration, and average CC of the example in Fig. 6 were 2.0×10^{15} Nm,
275 24 s, and 0.65, respectively. The seismic moment rate of the VLFE was obtained by dividing the
276 seismic moment by the source duration. We estimated the uncertainties of the VLFE moments by
277 using the nonparametric bootstrap method. First, 100 bootstrap samples were prepared for each
278 event. Since seven components are used for VLFE analysis (vertical component of N.KYKF and
279 radial and vertical components in other F-net stations shown in Fig. 6), a bootstrap sample
280 consisted of seven components including duplicates. Subsequently, VLFE moments were
281 calculated by using each bootstrap sample composed of seven components. Then, we estimated
282 the standard deviations of the 100 VLFE moments. The uncertainty of VLFE moments is 0.2–0.3
283 order (Fig. S3b).

284 The fit between the observed and simulated Love waves was not sufficient compared
285 with the Rayleigh wave (Fig. 6b). It may be inferred that the sedimentary structure of JIVSM at
286 very shallow depths (< 5 km) in Hyuga-nada is insufficient to simulate Love waves, which are
287 sensitive to shallow structures. We verified that the CCs between the simulated and observed
288 waveforms of a regular earthquake located by Takemura et al. (2020) in the transverse
289 components were also low, whereas those in the vertical and radial components were high (Fig.
290 S5). Therefore, we used only the vertical and radial components (Rayleigh waves) when
291 calculating the CCs. For the N.KYKF station, only the vertical component was utilized because
292 the horizontal components were noisy.

293



294

295

296 **Figure 6.** (a) VLFE source grids for the VLFE analysis. Crosses indicate the locations of the
 297 VLFE source grids. Purple crosses represents the grids with CC between synthetic and observed
 298 waveforms larger than 0.6. Gray dots indicate the epicentres of tremors detected by Yamashita et
 299 al. (2015; 2021). Red circle indicates the epicentre of the event displayed in Fig. 6b. Blue and
 300 brown triangles depict the locations of OBSs in 2013 and 2015, respectively. Dashed contours
 301 indicate the isodepth of the top of the Philippine Sea plate at 10-km intervals (JIVSM; Koketsu
 302 et al. 2012). Black line represents the trench axis. Inverted triangles display the locations of the
 303 F-net stations. (b) An example of a VLFE in a frequency range of 0.02–0.05 Hz. Waveforms are
 304 depicted from 17:04:21 (JST, UTC+9), May 31, 2015. Black and red lines are the observed and
 305 the simulated waveforms, respectively. R, T, and U components represent the radial, transverse,
 306 and vertical components, respectively.

307

308 3. Results

309 We estimated the energies of 1,672 and 6,126 shallow tremors in 2013 and 2015,
 310 respectively. We classified the analysis region into three areas based on spatial variation in
 311 energies of tremors and moments of VLFs (Figs 7 and S6): Area A, south of 31.0° N; Area B,
 312 west of 132.4°E, north of 31.0° N; and Area C, east of 132.4°E, north of 31.0° N (see rectangles
 313 of Fig. 7). Area A is south of the subducted Kyushu-Palau Ridge, Area B is near the top of the
 314 subducted ridge, and Area C is east of the subducted ridge. Most of Areas A and C are outside the
 315 subducted ridge. In 2013, tremors and VLFs occurred mainly in Areas A and B, whereas in 2015,
 316 they occurred mainly in Areas B and C. The dominant range of tremor energies was $10^{3.5}$ – $10^{7.5}$ J
 317 with spatial variation (Fig. 7ac). In 2013 (Fig. 7a), tremors with large energies ($> 10^6$ J) were
 318 concentrated in Area A. This characteristic is confirmed in the maximum and median values of
 319 tremor energies (Fig. S6a). In 2015 (Fig. 7c), tremors with larger energies ($> 10^{6.5}$ J) occurred
 320 near the north-eastern edge of the subducted Kyushu-Palau Ridge in Area C. The tremor energies
 321 near the trench axis in Area C were smaller. These characteristics are also shown in the maximum
 322 tremor energies (Fig. S6b). Although median tremor energies are small in the longitude of 132.5°–
 323 132.7° due to the detection of many small events, the north-eastern edge of the subducted Kyushu-
 324 Palau Ridge in Area C is considered as large tremor energy area.

325 The moments were also estimated for 1,297, 904, and 1,785 shallow VLFs in 2010,
 326 2013, and 2015, respectively. The dominant range of the VLFE moments was $10^{13.5}$ – $10^{16.5}$ Nm
 327 (Fig. 7b,d,e, and f). South of 31.0° N (Area A), VLFs with large moments ($> 10^{15.5}$ Nm) occurred
 328 in 2010 and 2013 (Fig. 7be). North of 31.0° N, VLFs extended near the trench axis in 2010 and
 329 2015. In particular, VLFs with large moments ($> 10^{15.5}$ Nm) in 2010 and 2015 (Figs 7de) are
 330 concentrated in east of 132.4° E (Area C). In the west of 132.4° E and north of 31.0° N (Area B),
 331 the VLFE moments are relatively small. These observations are stably confirmed in the maximum
 332 and median values of VLFE moments (Fig. S6c-f). The spatial variations in the VLFE moments
 333 and tremor energies for each observation period were similar (Fig. 7). The change in the maximum
 334 range of tremor energy or VLFE moment between Areas A and C and Area B is approximately
 335 one order (Fig. 7). Considering the uncertainty of tremor energies (0.5–1 orders) and VLFE
 336 moments (0.2–0.3 orders), the spatial variation in tremor energy and VLFE moment is considered
 337 to be real. The spatial variations in the energy rates of tremors and moment rates of VLFs were
 338 also approximately one order larger in Areas A and C than in Area B (Fig. S7). We summarized
 339 our observations: the energies of the tremors and moments of VLFs are generally larger outside
 340 the subducted ridge (Areas A and C) than near the top of the subducted ridge (Area B).

341 The spatiotemporal variation in moments and energies of slow earthquakes and the
 342 change in the migration speed are associated (Fig. 8a and b). Hereafter, we mainly discuss the
 343 spatiotemporal variation in slow earthquakes based on VLFE activity because the spatiotemporal

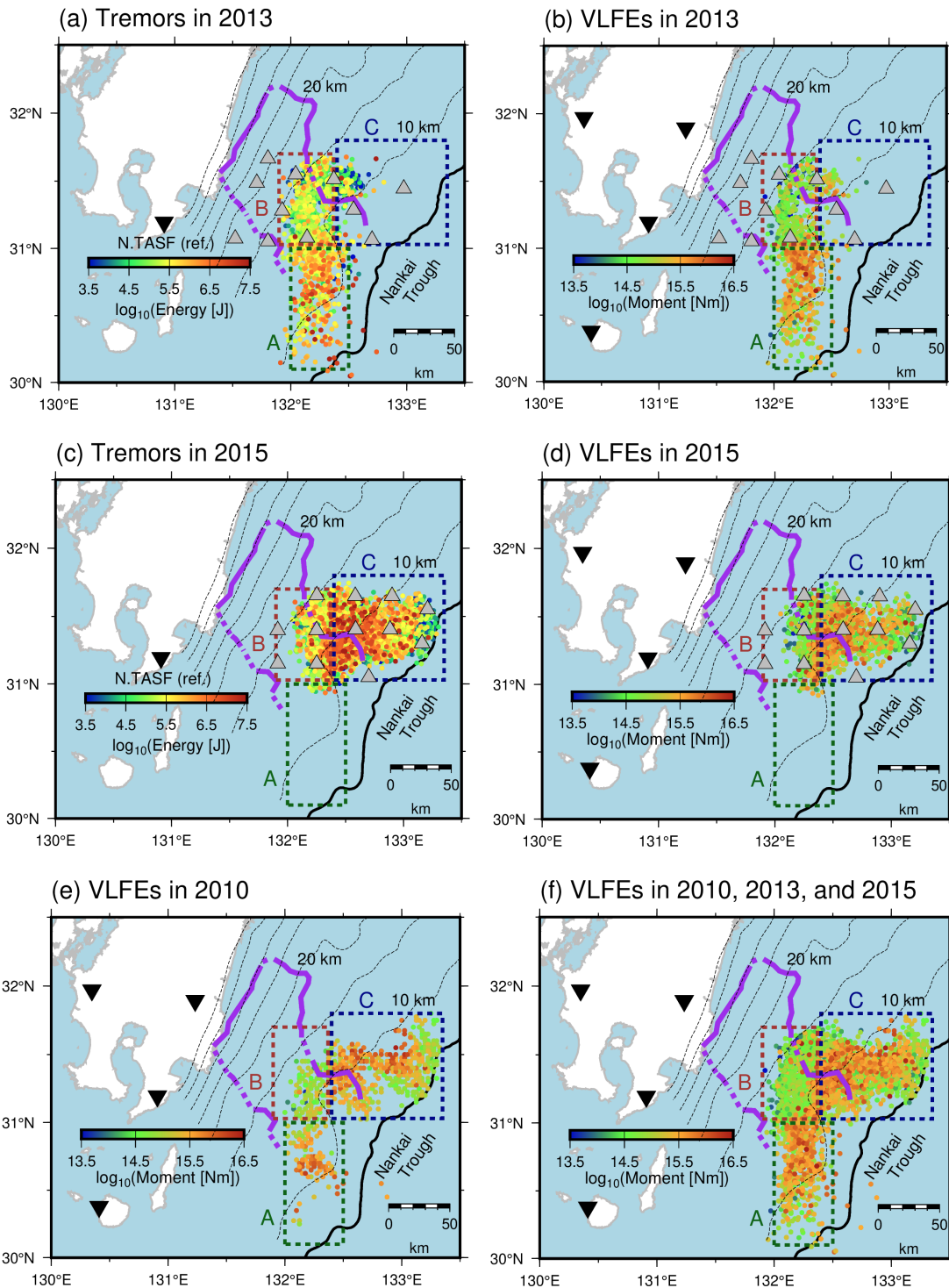
344 variations in VLFE moments and tremor energies were similar, and the VLFE analysis covered
345 all episodes in 2010, 2013, and 2015. Here, we summarized migration patterns in each episode.
346 Their detailed features were described in the previous studies (Asano et al. 2015; Yamashita et al.
347 2015; Yamashita et al. 2021). The episodes in 2010 and 2015 are divided into three migrations
348 and the 2013 episode is divided into two migrations (Fig. S8 and Table S1). The 2010a, 2013a,
349 and 2013b migrations were northward along the strike, whereas the 2010b, 2010c, 2015a, 2015b,
350 and 2015c migrations were along the dip with various directions (Figs 8 and S8; Table S1). All
351 migrations along the strike direction consistently started in Area A (Figs 8b, S8a, S8d, and S8e).
352 Subsequently, the VLFES migrated northward and entered the subducted ridge. After VLFES
353 entered Area B, their migration speed became slow (Fig. 8a and b). The spatiotemporal variation
354 in the migration front seems to be parabolic (discussed in detail in Section 4.1). Rapid tremor
355 reversals (RTRs; black dotted arrows in Figs 8b and S8d), which is a fast backward migration
356 (e.g., Houston et al. 2011), occurred during the migration in 2013.

357 In the main front of along-strike migrations, the moments of VLFES become smaller
358 after the front entered the Area B and the migration speed slowed (Figs 8b, S8a, S8d, and S8e).
359 Therefore, the migration speed and the moments of VLFES are positively correlated. On the other
360 hand, the moments of the VLFES in RTRs become larger when RTRs entered Area A (Figs 8b and
361 S9d). This suggests that the moments of VLFES depend on the location.

362 In the downdip of shallow tremors and VLFES, repeating earthquakes occurred at depths
363 of 15–30 km. The repeating earthquake activity manifests that the plate boundary around its patch
364 is creeping; therefore, the large slip rate by repeating earthquakes suggests that the interplate
365 coupling is weak (e.g., Uchida & Matsuzawa 2011). Fig. 9 compares the spatial distributions of
366 slip rates from repeating earthquakes and cumulative moments of VLFES. Cumulative moments
367 of VLFES may be also linked with the strength of interplate coupling (Baba *et al.* 2020). The
368 interplate slip rate estimated from repeating earthquakes was higher in the south along the strike
369 direction (Yamashita et al. 2012); therefore, the interplate coupling may be weaker at depths of
370 15–30 km in the south (downdip part of Area A) than in the north (downdip of Area B). The
371 cumulative moment of shallow VLFES in 2010 and 2013, episodes with along-strike migrations,
372 was also smaller in Area B than in Area A during the episodes (Fig. 9). Baba et al. (2020) found
373 the tendency that cumulative moment of shallow VLFES was larger in areas with weak interplate
374 coupling along the Nankai Trough. In Hyuga-nada, the slip rate of repeating earthquakes and the
375 cumulative moment of VLFES are larger in the south (in and downdip of Area A) than in the north
376 (in and downdip of Area B). These observations suggest that although there is a difference in the
377 slip behaviour along the dip direction, such as repeating earthquakes and VLFES, the interplate
378 coupling may be consistently weak in the south along the strike direction. Although Area C is the
379 northern part of Hyuga-nada, the cumulative moment of VLFES is large. Area C is apart from the

380 repeating earthquake area and close to the trench axis unlike Areas A and B; therefore, interplate
381 coupling may be different from Area B.
382

383



384

385

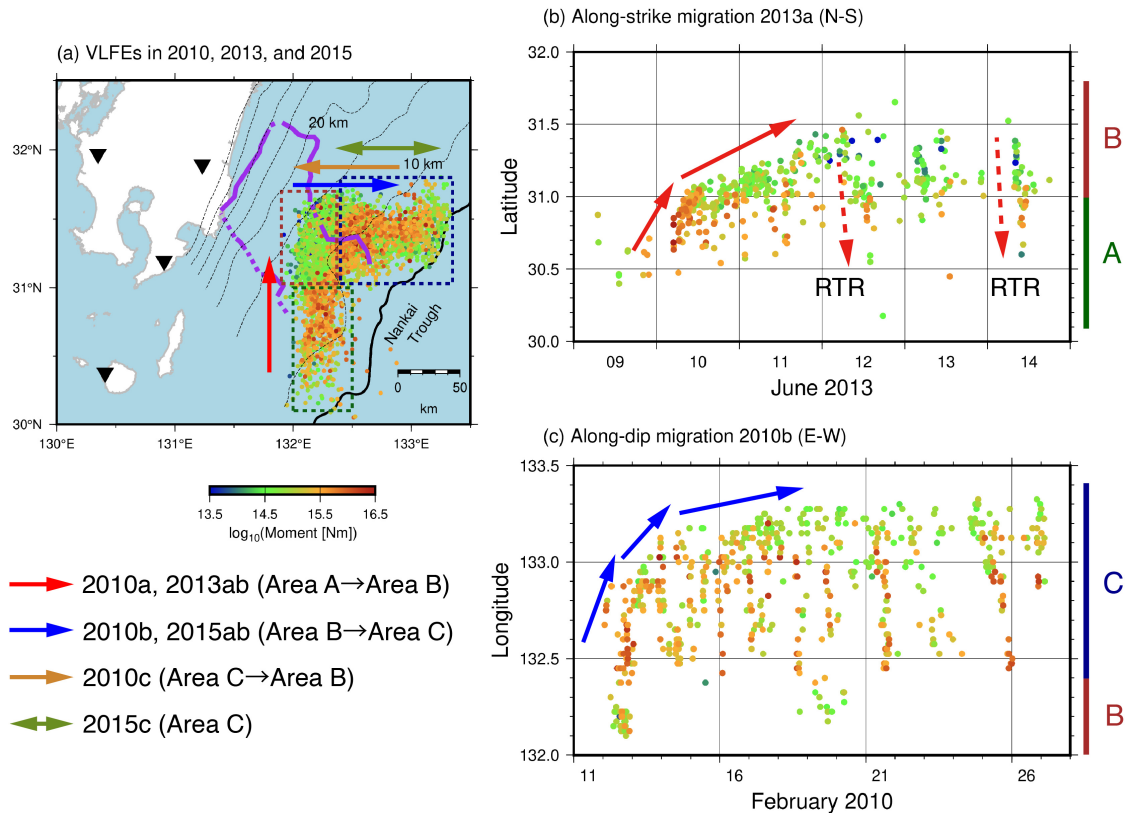
386

387

388

Figure 7. Spatial distribution of (a) energies of tremors in 2013, (b) moments of VLFs in 2013, (c) energies of tremors in 2015, (d) moments of VLFs in 2015, (e) moments of VLFs in 2010, and (f) moments of VLFs in all analysis periods. Green, brown, and dark blue dotted rectangles

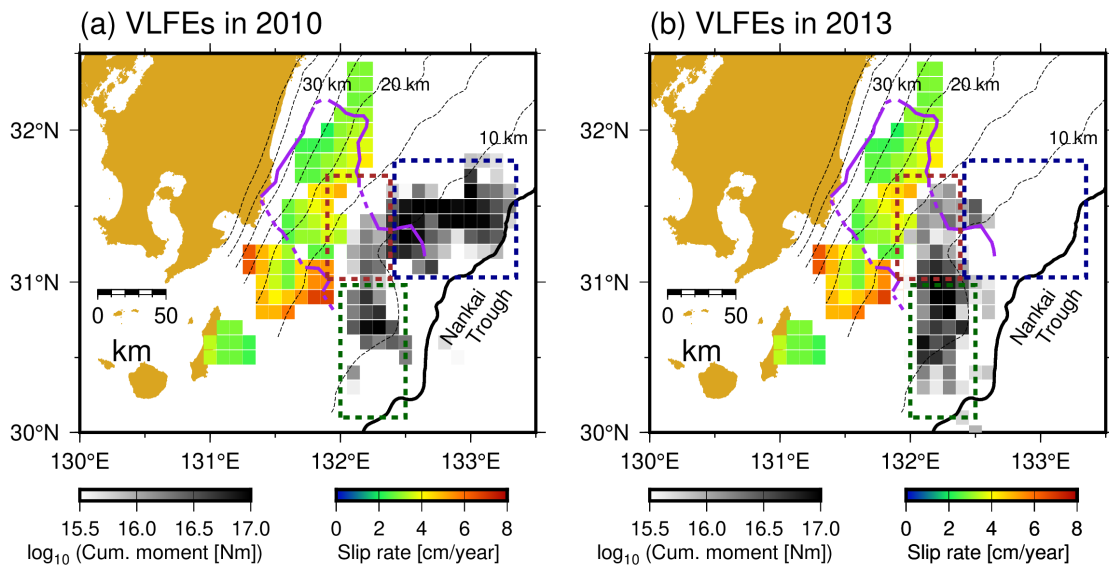
389 indicate the ranges of Area A, B, and C, respectively. Purple lines represent the inferred subducted
 390 Kyushu-Palau Ridge (Yamamoto *et al.* 2013). Gray triangles depict the locations of OBSs. Inverted
 391 triangles and black line are the same as displayed in Fig. 4. Dashed contours indicate the isodepth
 392 at the top of the Philippine Sea plate in intervals of 5 km (Nakanishi *et al.* 2018).
 393



394
 395

396 **Figure 8.** (a) Summary of slow earthquake migration patterns. Coloured arrows represent the
 397 direction of migration patterns. Coloured dotted rectangles, dashed contours, purple lines and
 398 black inverted triangles are the same as displayed in Fig. 7. (b) Spatiotemporal distributions of
 399 (b) an along-strike migration 2013a and (c) along-dip migration 2010b with moments of VLFEs.
 400 Black arrows indicate the direction of migrations. Black dotted arrows in Fig. 8b represents the
 401 RTR.

402
 403



404

405

406

407

408

409

410

411

Figure 9. Relationship between slip rates estimated from repeating earthquakes (Yamashita et al. 2012) and shallow slow earthquakes. Gray scales exhibit the cumulative moments of VLFEs. Colour scale indicates the slip rate estimated from repeating earthquakes. Coloured dotted rectangles, purple lines, black lines, and dashed contours are the same as in Fig. 7.

412 **4. Discussion**

413 **4.1. Along-strike spatial variation in slow earthquake activity**

414 To investigate the controlling factor of the along-strike variation in slow earthquake
415 activity in Hyuga-nada, we compared the activity with a physical model of along-strike slow
416 earthquake migration by Ando et al. (2012). In their model, high- and low-strength brittle tremor
417 patches exist on the ductile background based on Newtonian rheology. The rupture of these brittle
418 patches is triggered by the stress increase at the migration front of an SSE. They predicted that
419 tremors start migrating energetically in areas with high tremor-patch strength (strong patch areas)
420 and decelerates with a parabolic spatiotemporal pattern in areas with low tremor-patch strength
421 (weak patch areas). In Hyuga-nada, the migration speed was faster, and the VLFE moment was
422 larger in Area A than in Area B (Fig. 8). These observations are consistent with the modelling
423 results by Ando et al. (2012). The along-strike variation in slow earthquake activity in Hyuga-
424 nada can be explained by the difference in the patch strength of slow earthquakes, where Areas A
425 and B are considered strong and weak patch areas, respectively (Fig. 10).

426 The spatial variations in tremor activity in Shikoku and VLFE activity off the south-
427 eastern Kii Peninsula were also discussed based on Ando et al. (2012) (Shikoku: Kano et al.
428 2018b; off the southeast Kii Peninsula: Yamamoto et al. 2022). In Shikoku, western and central
429 Shikoku were interpreted as strong and weak patch areas, respectively, whereas the areas west of
430 and inside the subducted Paleo-Zenisu ridge off the Kii Peninsula were regarded as strong and
431 weak patch areas, respectively.

432 A possible factor for the along-strike spatial variation in slow earthquake activity in
433 Hyuga-nada is the heterogeneity of pore fluid pressure. Kano et al. (2018b) suggested that the
434 heterogeneity of strong and weak patch areas is caused by the variation in effective normal stress,
435 which is associated with that in the fluid pressure on the plate boundary. Takemura et al. (2022a)
436 discussed that the variation in the pore fluid pressure can induce the change of the migration speed,
437 which can be considered as a proxy for rupture propagation of an SSE (e.g., Bartlow et al. 2011;
438 Ito et al. 2007), off the Cape Muroto and Kii Peninsula. In Hyuga-nada, the change in migration
439 speed between Area A and B may be caused by the pore fluid pressure heterogeneity. To discuss
440 the variation in the pore fluid pressure in Hyuga-nada in more detail, investigations of seismic
441 velocity structures (especially V_S and V_P/V_S ratio) are required in future work.

442 Another possible factor is the geometrical effects of the subduction of a ridge. Wang
443 and Bilek (2011) suggested that a fracture network caused by a subducted seamount generates
444 structural and stress heterogeneities. According to Chesley et al. (2021), the subduction of a
445 seamount can transport considerable volume of fluid to forearc and complex fracture network,
446 which can generate the effective normal stress variation. Takemura et al. (2022b) and Yamamoto
447 et al. (2022) suggested the variation in cumulative moments of VLFEs which is associated with

448 subducted Paleo-Zenisu ridge off the Kii Peninsula. In Hyuga-nada, the subduction of the
449 Kyushu-Palau ridge may also generate the stress heterogeneity on the plate boundary.

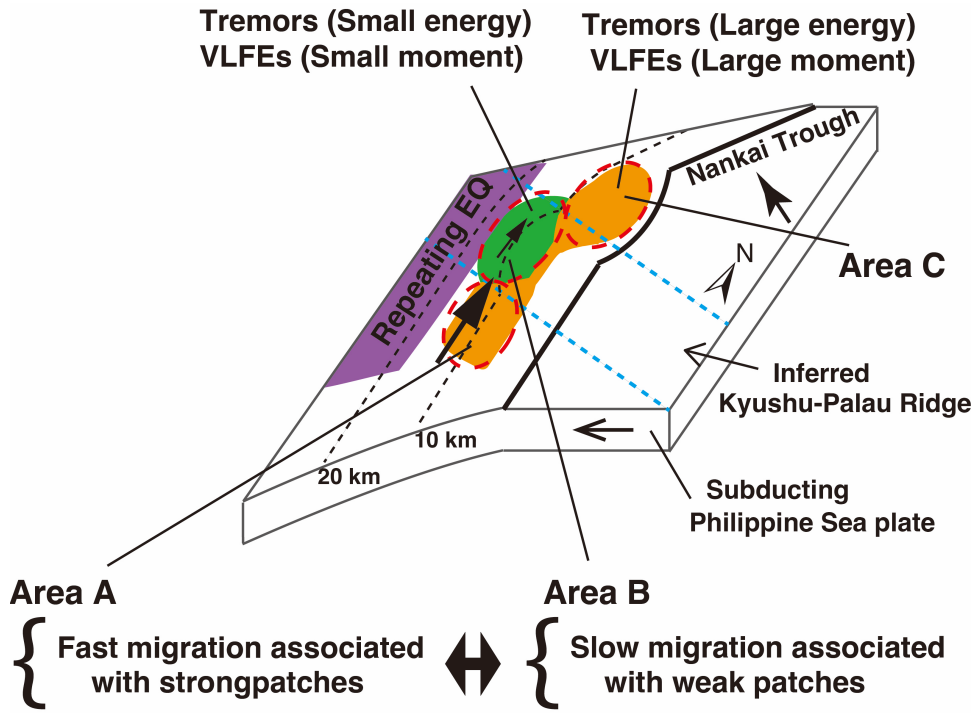
450 As mentioned in Section 3, the spatiotemporal variation in the migration front appears
451 to be parabolic. Following Ando et al. (2012), we investigated which function is better for fitting
452 the migration front in 2013a, exponential ($t = C \exp(a(x + x_1)) + t_1$; t is the elapsed time, x is
453 the migration distance, C , a , x_1 , and t_1 are constant) or parabolic ($t = D^{-1}(x + x_2)^2 + t_2$; D is the
454 diffusion coefficient, x_2 , and t_2 are constant). Although tremor epicentres were scattered around
455 the start of migration, the migration pattern seems to be better fitted by a parabola (Fig. 11) rather
456 than exponential, and the diffusion coefficient D is evaluated as $\sim 6 \times 10^4 \text{ m}^2/\text{s}$.

457 Ando et al. (2012) assumed that fault strength is equals to τ_p when slip velocity $v=0$ and
458 equals to $\tau_r + \eta v$ when $v > 0$ following Ando et al. (2010) and Nakata et al. (2011). τ_p , τ_r , η are peak
459 strength, residual strength, and viscosity factor, respectively. In Ando et al. (2012), τ_r is set as zero
460 and the patch strength is represented by τ_p . The difference in τ_p between strong and weak patches
461 is supposed to be represented by that in stress drop. Therefore, we roughly evaluated the variation
462 in the stress drop of the VLFEs in Hyuga-nada. Assuming a circular crack model, the seismic
463 moment M_0 of an earthquake is given by (e.g., Kanamori & Anderson 1975):

$$464 \quad M_0 = \frac{16}{7} \Delta \tau r^3 \quad (5)$$

465 where $\Delta \tau$ is the stress drop and r is the radius of the patch. In this section, this relationship is
466 further assumed in VLFEs. The average moment of a VLFE in Area A (strong patch area) and in
467 Area B (weak patch area) is $3.3 \times 10^{15} \text{ Nm}$ and $1.1 \times 10^{15} \text{ Nm}$, respectively (Fig. 7b, d, e, and f).
468 Considering Ohta & Ide (2017) estimated the source radius of a deep VLFE with $M_0 = 1.2 \times 10^{14} \text{ Nm}$
469 as $\sim 5 \text{ km}$, we assume the radius of a shallow VLFE patch in Hyuga-nada with $M_0 = 10^{13.5} - 10^{16.5}$ as
470 $3 - 30 \text{ km}$. If patches with a radius r of $3 - 30 \text{ km}$ are assumed, the average stress drop of a VLFE
471 in Areas A and B is evaluated as $5.3 \times 10^1 - 5.3 \times 10^4 \text{ Pa}$ and $1.8 \times 10^1 - 1.8 \times 10^4 \text{ Pa}$, respectively. The
472 spatiotemporal distribution of migration is parabolic if the difference in stress drop between
473 strong and weak patches is sufficient (Ando et al. 2012). As indicated by the fitting of the
474 migration front, the spatiotemporal variation in the slow earthquake migration front was parabolic
475 (Fig. 8b). Although the model of Ando et al. (2012) assumed an 11-times differences between
476 strong and weak patches, if the patch size in Areas A and B is similar, parabolic migration pattern
477 was observed by an approximately three-time difference in the stress drops of these patches in
478 Hyuga-nada. On the other hand, since the difference in the moment of VLFEs between Areas A
479 and B may be due to the patch size, slip distribution of VLFEs should be investigated in future
480 studies. However, the estimation of slip areas of shallow VLFEs is a challenging issue due to
481 offshore heterogeneities along the propagation path. The patch heterogeneity may be a key factor
482 of variations in tremor energy, VLFE moment, and migration speed in Hyuga-nada. Although we

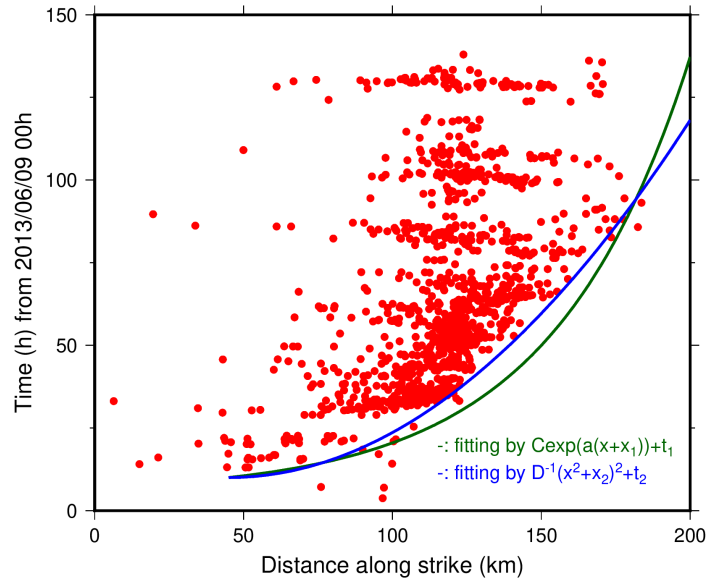
483 conducted a general classification of slow earthquake areas, more statistical approaches, such as
484 clustering procedures, may be useful to construct a new model of slow earthquake activity.
485



486
487

488 **Figure 10.** Schematic illustration of the interpretation of distributions of slow earthquakes and
489 Kyushu-Palau Ridge.

490
491
492
493



494

495

496 **Figure 11.** Spatiotemporal distribution of tremor migration in the episode of 2013a. Vertical and
497 horizontal axis shows the elapsed time from 2013/06/09 00:00:00 JST, and Distance along the
498 strike (N-S) from 30.0°N, respectively. Blue and green lines indicate the parabolic and exponential
499 curves, respectively.

500

501 **4.2. Scaled energy of shallow slow earthquakes in Hyuga-nada**

502 To discuss the characteristics of the source process of slow earthquakes in Hyuga-nada,
 503 we estimated the scaled energy following previous studies (e.g., Ide et al., 2008; Yabe et al., 2019;
 504 2021) using the ratio between the tremor energy rate and VLFE moment rate for activities in 2013
 505 and 2015, when the energy rate could be estimated from the OBS records. The dominant range of
 506 the scaled energy was $10^{-11.5}$ – $10^{-8.5}$ both in 2013 and 2015 (Fig. 12ab). Dominant ranges of scaled
 507 energies did not change significantly between episodes in 2013 and 2015 (Fig. S9). The range of
 508 the median scaled energy is in the range of $10^{-10.5}$ – $10^{-9.5}$ in all areas (Fig. 12cd). The median scaled
 509 energy is approximately 0.5 orders smaller around the eastern edge of the Kyushu-Palau Ridge in
 510 Area C than in other areas. However, the range of scaled energy is ranged to three to four orders
 511 in all areas (Fig. S9). In addition, the uncertainty of scaled energy often reaches approximately
 512 one order (Fig. S10). Therefore, it is difficult to consider that the 0.5 orders difference in median
 513 scaled energy in the western part of Area C is due to the variation in the rupture process in Hyuga-
 514 nada. The characteristics of the scaled energy do not change in spatially and temporally in the
 515 order scale inside the Hyuga-nada. Apparent stress is estimated by multiplying scaled energy by
 516 rigidity. Since the range of scaled energy is similar between Areas A and B, the apparent stress is
 517 similar if the rigidity is the same.

518 The range of scaled energies in Hyuga-nada is similar to or one order smaller compared
 519 to the off the Cape Muroto and Kii Peninsula (10^{-10} – 10^{-8} ; Yabe et al. 2021, 2019), along the Japan
 520 Trench (10^{-10} – 10^{-9} ; Yabe et al. 2021), and in Costa Rica (10^{-9} – 10^{-8} ; Baba et al. 2021). The range
 521 of scaled energies of shallow slow earthquakes in Hyuga-nada is also similar to those of deep
 522 slow earthquakes in southwest Japan, Cascadia, and Mexico ($10^{-9.5}$ – 10^{-9} ; Ide, 2016; Ide and Maury,
 523 2018; Ide and Yabe, 2014; Fig. 13). However, the range of scaled energy in Hyuga-nada is broader
 524 than other slow earthquake regions.

525 Ide (2008) and Ide & Maury (2018) discussed the theoretical relationship between
 526 seismic energy rate and seismic moment rate of slow earthquakes by the Brownian slow
 527 earthquake model. In their model, the characteristic size of the slip area S is described by:

528
$$S = Cr^2 \quad (6)$$

529 where r is a random variable and C is a constant. The temporal change of r is described by:

530
$$dr = -\alpha r dt + \sigma dB \quad (7)$$

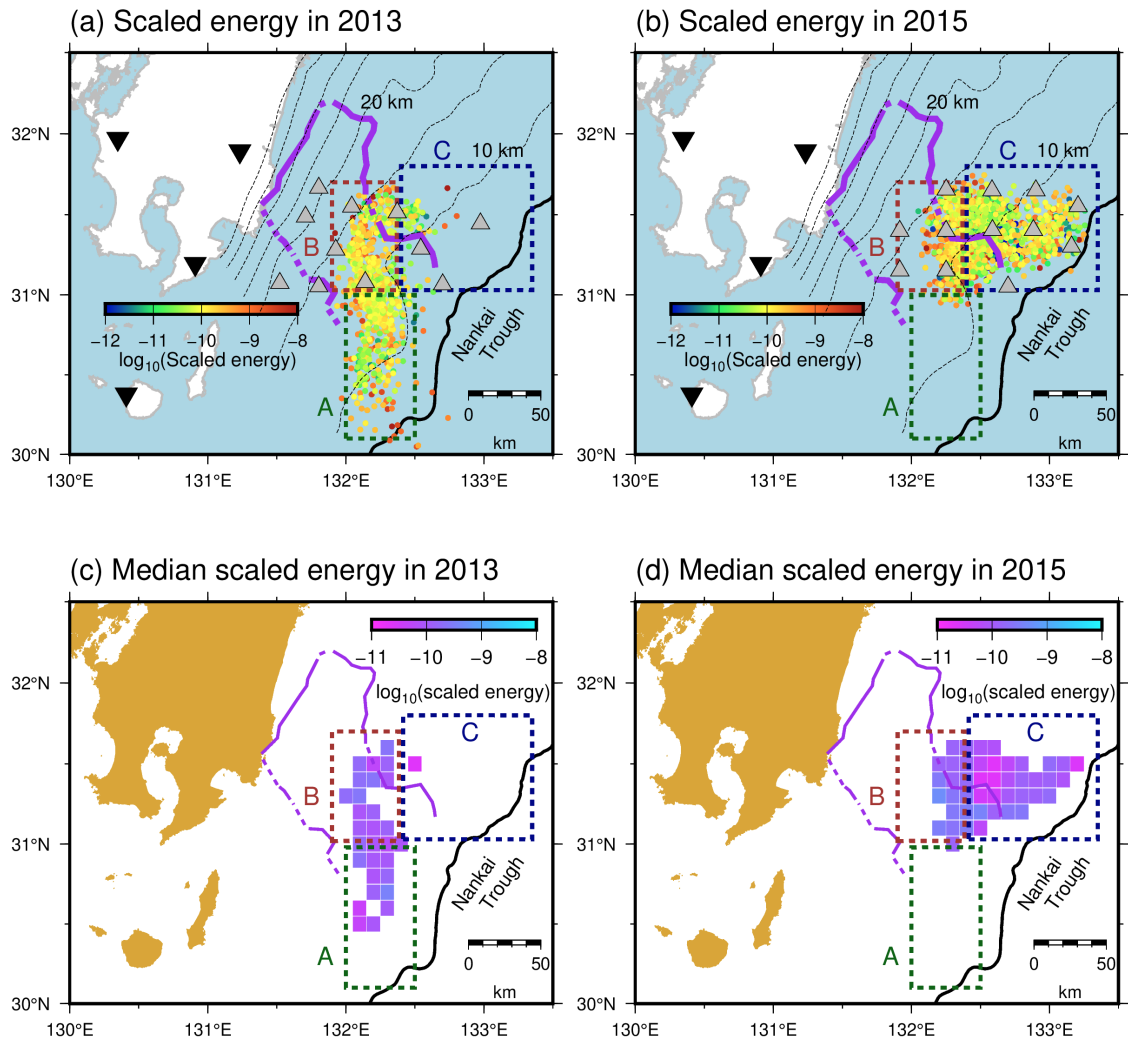
531 where α is the characteristic frequency of slow earthquakes (α^{-1} is a characteristic time), dB is the
 532 random variable of Gaussian distribution with the mean 0 and the variance 1, σ is the fluctuation
 533 magnitude. They discussed that the energy rate divided by the square of the moment rate depends
 534 on a characteristic frequency of a slow earthquake event, α :

535
$$\frac{E[E_{rate}]}{E[M_{rate}]^2} = \frac{4\alpha}{5\pi\rho V_s^5 \Delta t} \quad (8)$$

536 where ρ is the density, V_s is the S -wave velocity, and Δt is the time steps of the stochastic process.
537 $E[E_{rate}]$ and $E[M_{rate}]$ indicates the long-term averages of energy rates and moment rates,
538 respectively. Ide & Maury (2018) evaluated $E[E_{rate}]/E[M_{rate}]^2$ and α^{-1} of seismic slow earthquakes
539 in deep southwest Japan, Cascadia, and Mexico as 10^{-22} – 10^{-20} and 0.3–30 s, respectively. The
540 range of α^{-1} of the SSE scale in deep southwest Japan, Cascadia, and Mexico evaluated by Ide &
541 Maury (2018) is 75–300 s. $E[E_{rate}]/E[M_{rate}]^2$ in Hyuga-nada is estimated to be 10^{-25} – $10^{-21.5}$ (Fig.
542 S11). Although the small value of $E[E_{rate}]/E[M_{rate}]^2$ is possibly caused by because the ρ and/or V_s
543 may be smaller in Hyuga-nada, if ρ , V_s , and Δt is the same order as in the values of Ide & Maury
544 (2018), α^{-1} in Hyuga-nada is estimated to be 10–30000 s. In Hyuga-nada, there may be slow
545 earthquake events that have similar or longer characteristic times than those of other slow
546 earthquake regions. In addition, the range of the characteristic time is broader in Hyuga-nada than
547 in other slow earthquake regions; therefore, slow earthquakes in Hyuga-nada may have various
548 spectral features. Based on Ide & Maury (2018), the wide range of characteristic time in this area
549 suggests width variations of tremor source area.

550

551



552

553

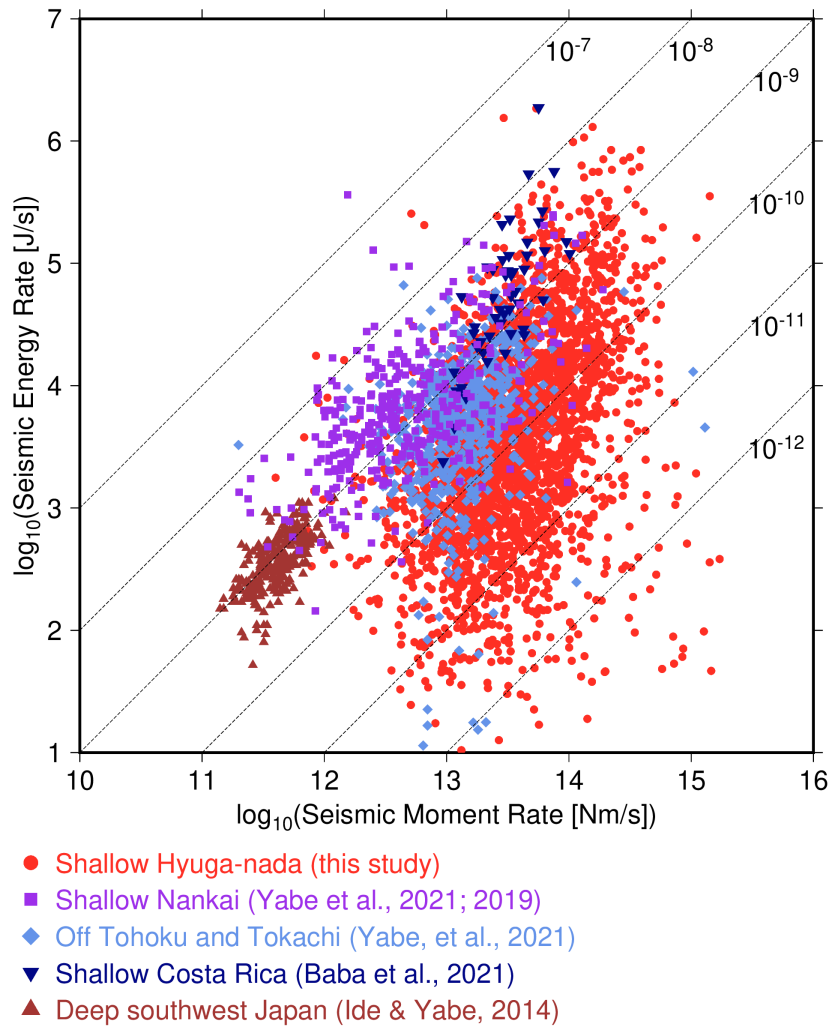
554 **Figure 12.** Spatial distribution of scaled energy of shallow slow earthquakes (a) in 2013 and (b)

555 in 2015. Spatial distribution of the median scaled energy in the grid of $1^\circ \times 1^\circ$ where the number

556 of event is larger than 10 (a) in 2013 and (b) in 2015. Coloured dotted rectangles, purple lines,

557 black lines, gray triangles, inverted triangles, and dashed contours are the same as in Fig. 7.

558



559

560

561 **Figure 13.** Relationship between seismic moment rates of VLFEs and seismic energy rates of
562 tremors. Red circles, purple squares, green diamonds, dark blue inverted triangles, and dark blue
563 triangles indicate the relationships between seismic moment rates of VLFEs and seismic moment
564 rates of tremors in shallow Hyuga-nada (this study), shallow Nankai except Hyuga-nada (Yabe *et*
565 *al.* 2019, 2021), off Tohoku and Tokachi (Yabe *et al.* 2021), shallow Costa Rica (Baba *et al.* 2021),
566 and deep slow earthquakes (Ide & Yabe 2014; Ide 2016; Ide & Maury 2018). Dashed lines represent
567 scaled energies of 10^{-7} , 10^{-8} , 10^{-9} , 10^{-10} , 10^{-11} , and 10^{-12} .

568

569 **5. Conclusion**

570 To investigate the spatial variation in the source characteristics of shallow slow
571 earthquakes in Hyuga-nada at a higher resolution, we estimated the energies of shallow tremors,
572 moments of shallow VLFES, and the scaled energy of shallow slow earthquakes in Hyuga-nada
573 using the data from permanent onshore broadband and temporary offshore seismometers. The
574 dominant ranges of energies of tremors and moments of VLFES are $10^{3.5}$ – $10^{7.5}$ J and $10^{13.5}$ – $10^{16.5}$
575 Nm, respectively. The energies of tremors and moments of VLFES are larger in Areas A and C
576 (most of which are outside the subducted Kyushu-Palau Ridge) than in Area B (near the top of
577 the subducted ridge). The migration of tremors and VLFES along the strike direction started in
578 Area A (south of the subducted ridge) with events of larger tremor energies and VLFE moments.
579 After going north and entering Area B (near the top of the subducted ridge), the migration speed
580 slowed, and the tremor energies and VLFE moments were observed to be small (Fig. 8b).

581 Based on the physical model of Ando et al. (2012), strengths of slow earthquake
582 patches in Areas A and B are expected to be strong and weak, respectively. The spatiotemporal
583 distribution of the tremor migration in 2013 is fitted by a parabolic function with the large energy
584 and moment events at the initiation of the migration in Area A. If a circular crack model and same
585 patch sizes are assumed, the difference in average stress drop of the VLFES in Area A (strong
586 patch) and Area B (weak patch) is evaluated as three times. This difference in the stress drop of
587 strong and weak patches may generate a parabolic migration pattern. The along-strike variation
588 in the rupture process on the plate boundary, such as the stress drop, in slow earthquake regions
589 can cause variations in the moment of slow earthquakes and migration pattern near the southern
590 edge of the subducted ridge.

591 The dominant range of scaled energy of slow earthquakes in Hyuga-nada is estimated
592 as $10^{-11.5}$ – $10^{-8.5}$. The range of scaled energies in Hyuga-nada is similar to or one order smaller than
593 other slow earthquake regions. Inside the Hyuga-nada, the spatial variation in scaled energy is not
594 found. Since the range of scaled energy is similar between Areas A and B, the apparent stress may
595 be similar if the rigidity is the same. Furthermore, this range is broader than other regions. Based
596 on the Brownian slow earthquake model by Ide & Maury (2018), the characteristic times of slow
597 earthquakes in Hyuga-nada (10–30000 s) is similar to or longer than those of other slow
598 earthquake regions (0.3–30 s). Following Ide & Maury (2018), the wide range of characteristic
599 time suggests the width variations of slow earthquake source area in Hyuga-nada. The slow
600 earthquakes in Hyuga-nada may have various spectral features.

601

602

603 **Acknowledgements**

604 We would like to thank the Editor Víctor M. Cruz-Atienza, the Assistant Editor Louise
605 Alexander, and two anonymous reviewers for their valuable comments and suggestions. We thank
606 Ryosuke Ando, Aitaro Kato, Satoshi Ide, Asuka Yamaguchi, Shoichi Yoshioka, Takashi Tonegawa,
607 Ryuta Arai, Masaru Nakano, Takane Hori, Eiichiro Araki, and Yojiro Yamamoto for their valuable
608 discussions. We appreciate Youichi Asano for providing the shallow VLFE data in 2010. This
609 research was supported by the JSPS KAKENHI Grant in Science Research on Innovative Areas
610 “Science of Slow Earthquakes” (JP16H06472), Grant-in-Aid for Scientific Research on
611 Transformative Research Areas (A) “Science of Slow-to-Fast earthquakes” (JP21H05205), and
612 JSPS Research Fellowship DC1 (JP19J20760). This study was also supported by the ERI JURP
613 2021-S-B102. This research is part of Satoru Baba’s PhD thesis (Baba, 2022).

614

615 **Author contribution statement**

616 SB conducted analysis and drafted the manuscript. SB, ST, KO, TA, YY, and MS
617 contributed the interpretation of this study. YY and MS designed the ocean bottom seismometer
618 observation. All authors read and approved the manuscript.

619

620 **Data availability statement**

621 A part of OBS data for this study was acquired by “Research project for compound
622 disaster mitigation on the great earthquakes and tsunamis around the Nankai Trough region,” a
623 project of the Ministry of Education, Culture, Sports, Science and Technology, Japan. The OBS
624 data is available from the corresponding author upon request. We used the F-net broadband
625 seismograms from the National Research Institute for Earth and Disaster Resilience (2019) and
626 the earthquake catalogues from the Japan Meteorological Agency
627 (https://www.data.jma.go.jp/svd/eqev/data/bulletin/index_e.html). OpenSWPC code Version
628 5.0.2 (Maeda *et al.* 2017) was utilized to calculate synthetic waveforms. We used the Fujitsu
629 PRIMERGY CX600M1/CX1640M1 (Oakforest-PACS) at the Information Technology Center,
630 the University of Tokyo for numerical simulations. Generic mapping tools (Wessel *et al.* 2013)
631 and the Seismic Analysis Code (Helfrich *et al.*, 2013) are used to prepare figures and process
632 seismograms, respectively. Catalogues of shallow tremors detected by Yamashita *et al.* (2015;
633 2021) can be downloaded from the Slow Earthquake Database (Kano, *et al.* 2018a). The estimated
634 tremor energies and VLFE moments are provided in an open access repository, zenodo
635 (<https://doi.org/10.5281/zenodo.8220097>).

636

637

638

639 **References**

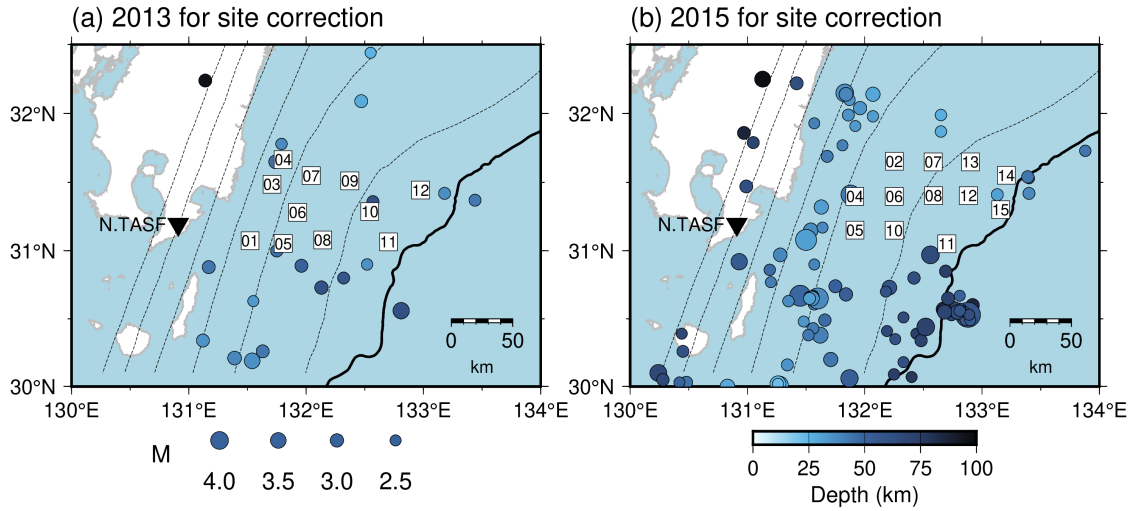
- 640 Amante, C., & Eakins, B.W. 2009. ETOPO1 1 Arc-Minute Global Relief Model: Procedures, Data
641 Sources and Analysis. NOAA Technical Memorandum NESDIS NGDC-24.
642 <https://doi.org/10.7289/V5C8276M>
- 643 Ando, R., Nakata, R. & Hori, T., 2010. A slip pulse model with fault heterogeneity for low-
644 frequency earthquakes and tremor along plate interfaces. *Geophys Res Lett*, **37**, 1–5.
645 doi:10.1029/2010GL043056
- 646 Ando, R., Takeda, N. & Yamashita, T., 2012. Propagation dynamics of seismic and aseismic slip
647 governed by fault heterogeneity and Newtonian rheology. *Journal of Geophysical Research B:
648 Solid Earth*, **117**, Blackwell Publishing Ltd. doi:10.1029/2012JB009532
- 649 Aoi, S., Asano, Y., Kunugi, T., Kimura, T., Uehira, K., Takahashi, N., Ueda, H., *et al.*, 2020.
650 MOWLAS: NIED observation network for earthquake, tsunami and volcano. *Earth, Planets and
651 Space*, **72**, Springer Berlin Heidelberg. doi:10.1186/s40623-020-01250-x
- 652 Asano, Y., Obara, K., Matsuzawa, T., Hirose, H. & Ito, Y., 2015. Possible shallow slow slip events in
653 Hyuga-nada, Nankai subduction zone, inferred from migration of very low frequency
654 earthquakes. *Geophys Res Lett*, **42**, 331–338. doi:10.1002/2014GL062165
- 655 Baba, S., 2022. Spatiotemporal characteristics of slow earthquakes in subduction zones around Japan.
656 PhD thesis of the University of Tokyo, Japan.
- 657 Baba, S., Obara, K., Takemura, S., Takeo, A. & Abers, G.A., 2021. Shallow Slow Earthquake Episodes
658 Near the Trench Axis Off Costa Rica. *J Geophys Res Solid Earth*. doi:10.1029/2021JB021706
- 659 Baba, S., Takemura, S., Obara, K. & Noda, A., 2020. Slow Earthquakes Illuminating Interplate
660 Coupling Heterogeneities in Subduction Zones. *Geophys Res Lett*, **47**, 4–5.
661 doi:10.1029/2020GL088089
- 662 Bartlow, N.M., Miyazaki, S., Bradley, A.M. & Segall, P., 2011. Space-time correlation of slip and
663 tremor during the 2009 Cascadia slow slip event. *Geophys Res Lett*, **38**, Blackwell Publishing
664 Ltd. doi:10.1029/2011GL048714
- 665 Chesley, C., Naif, S., Key, K. & Bassett, D., 2021. Fluid-rich subducting topography generates
666 anomalous forearc porosity. *Nature*, **595**, 255–260, Nature Research. doi:10.1038/s41586-021-
667 03619-8
- 668 DeMets, C., Gordon, R.G., Argus, D.F. & Stein, S., 1994. Effect of recent revisions to the geomagnetic
669 reversal time scale on estimates of current plate motions. *Geophys Res Lett*, **21**, 2191–2194.
670 doi:10.1029/94GL02118
- 671 Dragert, H., Wang, K., James, T.S., 2001. A Silent Slip Event on the Deeper Cascadia Subduction
672 Interface. *Science (1979)*, **292**, 1525–1528. doi:10.1126/science.1060152
- 673 Helffrich, G., Wookey, J., & Bastow, I. (2013). *The Seismic Analysis Code*. Cambridge: Cambridge
674 University Press. <https://doi.org/10.1017/CBO9781139547260>

- 675 Hirose, H., Hirahara, K., Kimata, F., Fujii, N. & Miyazaki, S., 1999. A slow thrust slip event following
676 the two 1996 Hyuganada earthquakes beneath the Bungo Channel, southwest Japan. *Geophys*
677 *Res Lett*, **26**, 3237–3240. doi:10.1029/1999GL010999
- 678 Houston, H., Delbridge, B.G., Wech, A.G., & Creager, K.C. 2011. Rapid tremor reversals in Cascadia
679 generated by a weakened plate interface. *Nature Geoscience*, **4**, 404-409,
680 doi:10.1038/NGE01157
- 681 Ide, S., 2016. Characteristics of slow earthquakes in the very low frequency band: Application to the
682 Cascadia subduction zone. *J Geophys Res Solid Earth*, **121**, 5942–5952.
683 doi:10.1002/2016JB013085
- 684 Ide, S. & Beroza, G.C., 2001. Does apparent stress vary with earthquake size? *Geophys Res Lett*, **28**,
685 3349–3352.
- 686 Ide, S., Beroza, G.C., Shelly, D.R. & Uchide, T., 2007. A scaling law for slow earthquakes. *Nature*,
687 **447**, 76–79. doi:10.1038/nature05780
- 688 Ide, S., Imanishi, K., Yoshida, Y., Beroza, G.C. & Shelly, D.R., 2008. Bridging the gap between
689 seismically and geodetically detected slow earthquakes. *Geophys Res Lett*, **35**, 2–7.
690 doi:10.1029/2008GL034014
- 691 Ide, S. & Maury, J., 2018. Seismic Moment, Seismic Energy, and Source Duration of Slow
692 Earthquakes: Application of Brownian slow earthquake model to three major subduction zones.
693 *Geophys Res Lett*, **45**, 3059–3067. doi:10.1002/2018GL077461
- 694 Ide, S. & Yabe, S., 2014. Universality of slow earthquakes in the very low frequency band. *Geophys*
695 *Res Lett*, **41**, 2786–2793. doi:10.1002/2014GL059712
- 696 Igarashi, T., 2020. Catalog of small repeating earthquakes for the Japanese Islands. *Earth, Planets and*
697 *Space*, **72**, Springer Berlin Heidelberg. doi:10.1186/s40623-020-01205-2
- 698 Ito, Y., Obara, K., Shiomi, K., Sekine, S. & Hirose, H., 2007. Slow Earthquakes Coincident with
699 Episodic Tremors and Slow Slip Events. *Science (1979)*, **315**, 503–506.
700 doi:10.1126/science.1134454
- 701 Kanamori, H. & Anderson, D.L., 1975. THEORETICAL BASIS OF SOME EMPIRICAL
702 RELATIONS IN SEISMOLOGY. *Bulletin of the Seismological Society of America*, Vol. 65.
703 Retrieved from [http://pubs.geoscienceworld.org/ssa/bssa/article-](http://pubs.geoscienceworld.org/ssa/bssa/article-pdf/65/5/1073/5320189/bssa0650051073.pdf)
704 [pdf/65/5/1073/5320189/bssa0650051073.pdf](http://pubs.geoscienceworld.org/ssa/bssa/article-pdf/65/5/1073/5320189/bssa0650051073.pdf)
- 705 Kanamori, H. & Rivera, L., 2006. Energy partitioning during an earthquake. *Geophysical Monograph*
706 *Series*, **170**, 3–13. doi:10.1029/170GM03
- 707 Kaneko, L., Ide, S. & Nakano, M., 2018. Slow Earthquakes in the Microseism Frequency Band (0.1–
708 1.0 Hz) off Kii Peninsula, Japan. *Geophys Res Lett*, **45**, 2618–2624. doi:10.1002/2017GL076773
- 709 Kano, M., Aso, N., Matsuzawa, T., Ide, S., Annoura, S., Arai, R., Baba, S., *et al.*, 2018a. Development
710 of a Slow Earthquake Database. *Seismological Research Letters*, **89**, 1566–1575.

- 711 doi:10.1785/0220180021
- 712 Kano, M., Kato, A., Ando, R. & Obara, K., 2018b. Strength of tremor patches along deep transition
713 zone of a megathrust. *Sci Rep*, **8**, Nature Publishing Group. doi:10.1038/s41598-018-22048-8
- 714 Kato, A., Obara, K., Igarashi, T., Tsuruoka, H., Nakagawa, S. & Hirata, N., 2012. Propagation of Slow
715 Slip Leading Up to the 2011 Mw 9.0 Tohoku-Oki Earthquake. *Science (1979)*, **335**, 705–708.
716 doi:10.1126/science.1215141
- 717 Koketsu, K., Miyake, H., Suzuki, H., 2012. Japan Integrated Velocity Structure Model Version 1. In:
718 Proceedings of the 15th World Conference on Earthquake Engineering, Lisbon, Portugal, 24-28
719 September, Paper 1773.
- 720 Maeda, T., Takemura, S. & Furumura, T., 2017. OpenSWPC: An open-source integrated parallel
721 simulation code for modeling seismic wave propagation in 3D heterogeneous viscoelastic media
722 4. *Seismology. Earth, Planets and Space*, **69**, Springer Berlin Heidelberg. doi:10.1186/s40623-
723 017-0687-2
- 724 Masuda, K., Ide, S., Ohta, K. & Matsuzawa, T., 2020. Bridging the gap between low-frequency and
725 very-low-frequency earthquakes. *Earth, Planets and Space*, **72**, Springer Berlin Heidelberg.
726 doi:10.1186/s40623-020-01172-8
- 727 Nadeau, R.M. & McEvilly, T. v, 1999. Fault Slip Rates at Depth from Recurrence Intervals of
728 Repeating Microearthquakes. *A. A. Koulakov and B. I. Shklovskii Phys. Rev. B*, Vol. 27.
- 729 Nakanishi, A., Takahashi, N., Yamamoto, Y., Takahashi, T., Citak, S.O., Nakamura, T., Obana, K., *et*
730 *al.*, 2018. Three-dimensional plate geometry and P-wave velocity models of the subduction zone
731 in SW Japan: Implications for seismogenesis. *Special Paper of the Geological Society of*
732 *America*, **534**, 69–86, Geological Society of America. doi:10.1130/2018.2534(04)
- 733 Nakata, R., Ando, R., Hori, T. & Ide, S., 2011. Generation mechanism of slow earthquakes: Numerical
734 analysis based on a dynamic model with brittle-ductile mixed fault heterogeneity. *J Geophys Res*
735 *Solid Earth*, **116**, Blackwell Publishing Ltd. doi:10.1029/2010JB008188
- 736 National Research Institute for Earth Science and Disaster Resilience, 2019. NIED F-net.
737 <https://doi.org/10.17598/NIED.0005>
- 738 Obara, K., 2002. Nonvolcanic Deep Tremor Associated with Subduction in Southwest Japan. *Science*
739 *(1979)*, **296**, 1679–1681. doi:10.1126/science.1070378
- 740 Obara, K. & Ito, Y., 2005. Very low frequency earthquakes excited by the 2004 off Kii peninsula
741 earthquakes: A dynamic deformation process in the large accretionary prism. *Earth, Planets and*
742 *Space*, **57**, 321–326. doi:10.1186/BF03352570
- 743 Obara, K. & Kato, A., 2016. Connecting slow earthquakes to huge earthquakes. *Science*, **353**, 253–
744 257. doi:10.1126/science.aaf1512
- 745 Ohta, K. & Ide, S., 2017. Resolving the Detailed Spatiotemporal Slip Evolution of Deep Tremor in
746 Western Japan. *J Geophys Res Solid Earth*, **122**, 10,009-10,036. doi:10.1002/2017JB014494

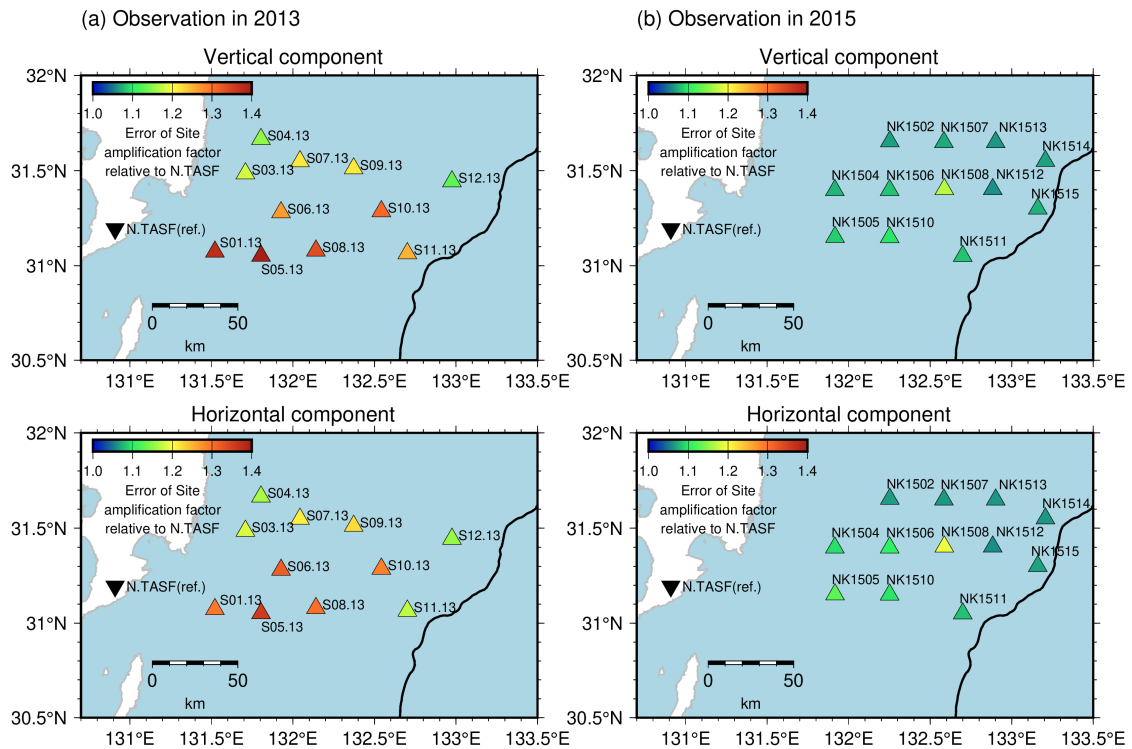
- 747 Rogers, G. & Dragert, H., 2003. Episodic Tremor and Slip on the Cascadia Subduction Zone: The
748 Chatter of Silent Slip. *Science (1979)*, **300**, 1942–1943. doi:10.1126/science.1084783
- 749 Shelly, D.R., Beroza, G.C., Ide, S. & Nakamura, S., 2006. Low-frequency earthquakes in Shikoku,
750 Japan, and their relationship to episodic tremor and slip. *Nature*, **442**, 188–191.
751 doi:10.1038/nature04931
- 752 Takemoto, T., Furumura, T., Saito, T., Maeda, T. & Noguchi, S., 2012. Spatial- and frequency-
753 dependent properties of site amplification factors in Japan derived by the coda normalization
754 method. *Bulletin of the Seismological Society of America*, **102**, 1462–1476.
755 doi:10.1785/0120110188
- 756 Takemura, S., Baba, S., Yabe, S., Emoto, K., Shiomi, K. & Matsuzawa, T., 2022a. Source
757 Characteristics and Along-Strike Variations of Shallow Very Low Frequency Earthquake
758 Swarms on the Nankai Trough Shallow Plate Boundary. *Geophys Res Lett*, **49**, John Wiley and
759 Sons Inc. doi:10.1029/2022GL097979
- 760 Takemura, S., Matsuzawa, T., Noda, A., Tonegawa, T., Asano, Y., Kimura, T. & Shiomi, K., 2019.
761 Structural Characteristics of the Nankai Trough Shallow Plate Boundary Inferred From Shallow
762 Very Low Frequency Earthquakes. *Geophys Res Lett*, **46**, 4192–4201.
763 doi:10.1029/2019GL082448
- 764 Takemura, S., Obara, K., Shiomi, K. & Baba, S., 2022b. Spatiotemporal Variations of Shallow Very
765 Low Frequency Earthquake Activity Southeast Off the Kii Peninsula, Along the Nankai Trough,
766 Japan. *J Geophys Res Solid Earth*, **127**, John Wiley and Sons Inc. doi:10.1029/2021JB023073
- 767 Takemura, S., Okuwaki, R., Kubota, T., Shiomi, K., Kimura, T. & Noda, A., 2020. Centroid moment
768 tensor inversions of offshore earthquakes using a three-dimensional velocity structure model:
769 slip distributions on the plate boundary along the Nankai Trough. *Geophys J Int*, **222**, 1109–
770 1125, Oxford University Press. doi:10.1093/gji/ggaa238
- 771 Tonegawa, T., Yamashita, Y., Takahashi, T., Shinohara, M., Ishihara, Y., Kodaira, S. & Kaneda, Y.,
772 2020. Spatial relationship between shallow very low frequency earthquakes and the subducted
773 Kyushu-Palau Ridge in the Hyuga-nada region of the Nankai subduction zone. *Geophys J Int*,
774 1542–1554, Oxford University Press. doi:10.1093/gji/ggaa264
- 775 Uchida, N. & Matsuzawa, T., 2011. Coupling coefficient, hierarchical structure, and earthquake cycle
776 for the source area of the 2011 off the Pacific coast of Tohoku earthquake inferred from small
777 repeating earthquake data. *Earth, Planets and Space*, **63**, 675–679, Springer Berlin.
778 doi:10.5047/eps.2011.07.006
- 779 Uchida, N., Matsuzawa, T., Hasegawa, A. & Igarashi, T., 2003. Interplate quasi-static slip off Sanriku,
780 NE Japan, estimated from repeating earthquakes. *Geophys Res Lett*, **30**, American Geophysical
781 Union. doi:10.1029/2003GL017452
- 782 Vaca, S., Vallée, M., Nocquet, J.M., Battaglia, J. & Régnier, M., 2018. Recurrent slow slip events as a

- 783 barrier to the northward rupture propagation of the 2016 Pedernales earthquake (Central
784 Ecuador). *Tectonophysics*, **724–725**, 80–92, Elsevier. doi:10.1016/j.tecto.2017.12.012
- 785 Wang, K. & Bilek, S.L., 2011. Do subducting seamounts generate or stop large earthquakes? *Geology*,
786 **39**, 819–822, Geological Society of America. doi:10.1130/G31856.1
- 787 Wessel, P., Smith, W.H.F., Scharroo, R., Luis, J. & Wobbe, F., 2013. Generic mapping tools: Improved
788 version released. *Eos (Washington DC)*, **94**, 409–410. doi:10.1002/2013EO450001
- 789 Yabe, S., Baba, S., Tonegawa, T., Nakano, M. & Takemura, S., 2021. Seismic energy radiation and
790 along-strike heterogeneities of shallow tectonic tremors at the Nankai Trough and Japan Trench.
791 *Tectonophysics*, 228714, Elsevier B.V. doi:10.1016/j.tecto.2020.228714
- 792 Yabe, S., Tonegawa, T. & Nakano, M., 2019. Scaled Energy Estimation for Shallow Slow Earthquakes.
793 *J Geophys Res Solid Earth*, **124**, 1507–1519. doi:10.1029/2018JB016815
- 794 Yamamoto, Y., Ariyoshi, K., Yada, S., Nakano, M. & Hori, T., 2022. Spatio-temporal distribution of
795 shallow very-low-frequency earthquakes between December 2020 and January 2021 in
796 Kumano-nada, Nankai subduction zone, detected by a permanent seafloor seismic network.
797 *Earth, Planets and Space*, **74**, 14. doi:10.1186/s40623-022-01573-x
- 798 Yamamoto, Y., Obana, K., Takahashi, T., Nakanishi, A., Kodaira, S. & Kaneda, Y., 2013. Imaging of
799 the subducted kyushu-palau ridge in the hyuga-nada region, western nankai trough subduction
800 zone. *Tectonophysics*, **589**, 90–102. doi:10.1016/j.tecto.2012.12.028
- 801 Yamashita, Y, Asano, Y., Shimizu, H., Uchida, K., Hirano, S., Umakoshi, K., Miyamachi, H., *et al.*,
802 2015. Migrating tremor off southern Kyushu as evidence for slow slip of a shallow subduction
803 interface. *Science (1979)*, **348**, 676–679. doi:10.1126/science.aaa4242
- 804 Yamashita, Y., Shimizu, H. & Goto, K., 2012. Small repeating earthquake activity, interplate quasi-
805 static slip, and interplate coupling in the Hyuga-nada, southwestern Japan subduction zone.
806 *Geophys Res Lett*, **39**, Blackwell Publishing Ltd. doi:10.1029/2012GL051476
- 807 Yamashita, Y., Shinohara, M. & Yamada, T., 2021. Shallow tectonic tremor activities in Hyuga-nada,
808 Nankai subduction zone, based on long-term broadband ocean bottom seismic observations.
809 *Earth, Planets and Space*, **73**, 196. doi:10.1186/s40623-021-01533-x
- 810
- 811



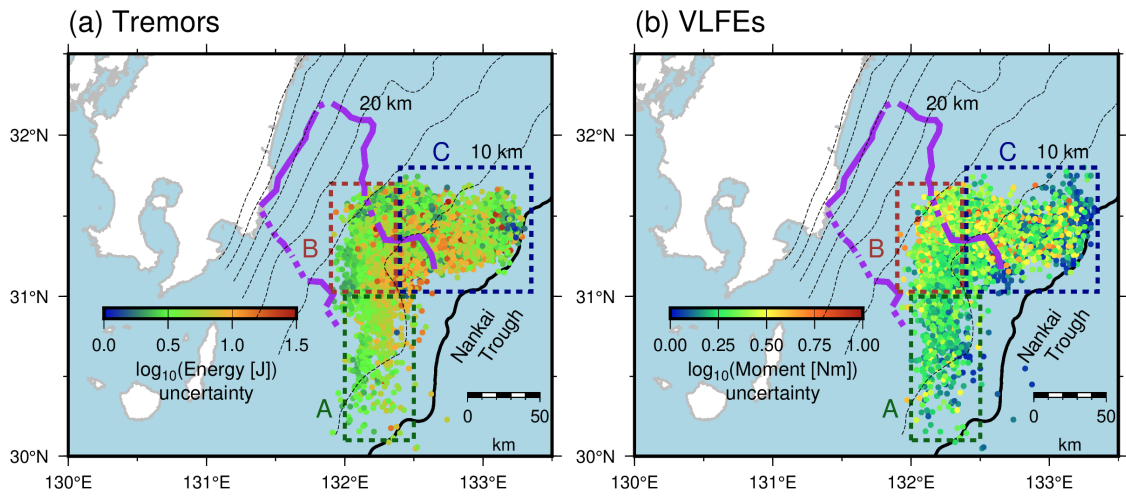
812
813
814
815
816

Figure S1. Distribution of earthquakes used for the estimation of the site amplification factors. Inverted triangles display the locations of the F-net stations. Squares represents the locations of OBSs. Black line and dotted contours are the same as displayed in Fig. 6.



817
818
819
820
821
822

Figure S2. Estimation errors of site amplification factors relative to N.TASF at each OBS. Inverted triangle indicates the location of the F-net station, N.TASF. Black line is the same as displayed in Fig. 3.

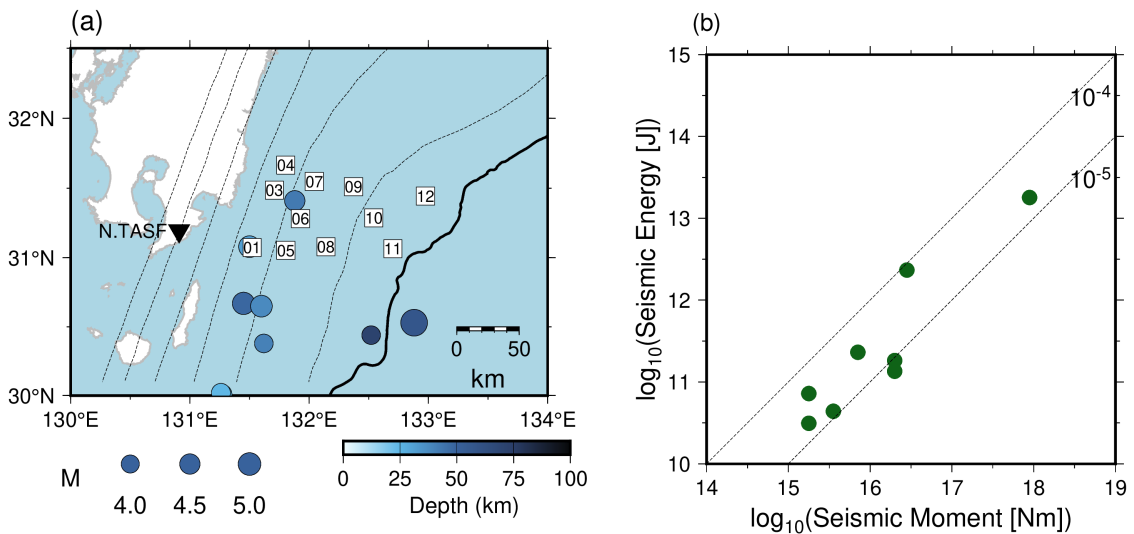


823

824

825 **Figure S3.** Spatial distribution of the uncertainty of logarithm of (a) tremor energies and (b) VLF E
 826 moments. Colored dotted rectangles, dashed contours, purple lines, black line and gray triangles
 827 are the same as displayed in Fig. 7.

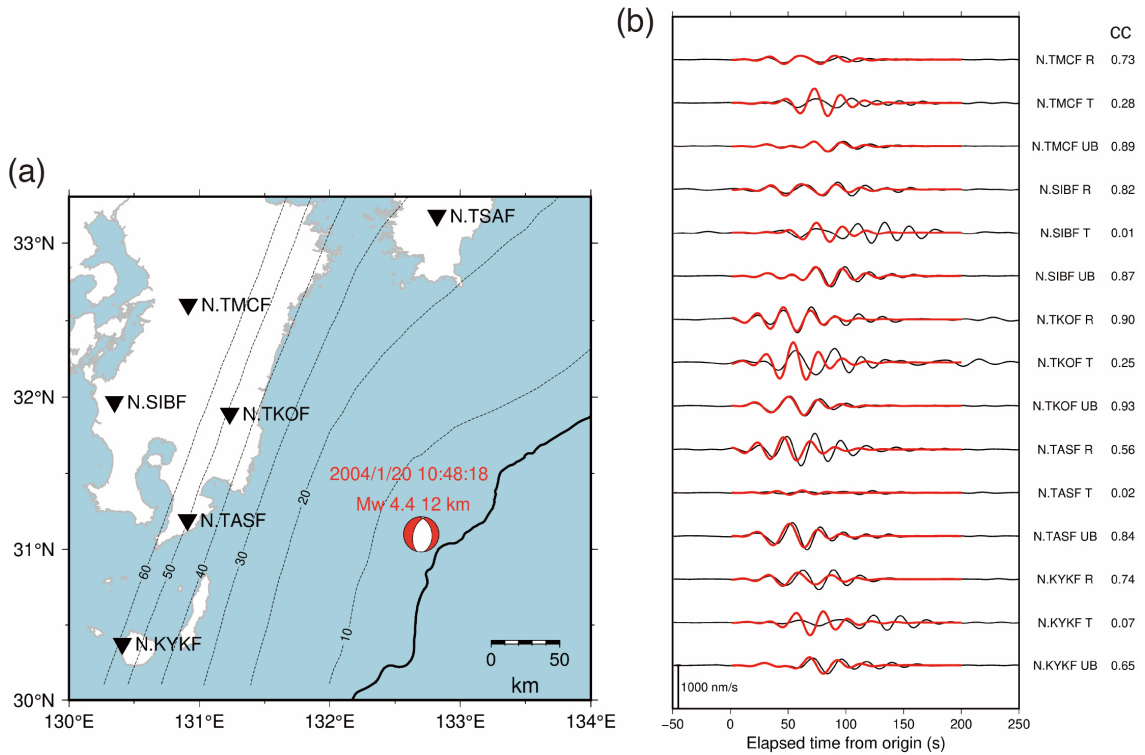
828



829

830

831 **Figure S4.** Estimation of seismic energies of regular earthquakes. (a) Distribution of earthquakes
 832 used for the estimation of seismic energies. Squares are the same as displayed in Fig. S1. Black
 833 line and dotted contours are the same as displayed in Fig. 6. (b) Relationship between seismic
 834 moment and seismic energy of earthquakes shown in Fig. S4a. Seismic moments are calculated
 835 from moment magnitude estimated by moment tensor analysis by F-net site
 836 (<https://www.fnet.bosai.go.jp/event/search.php?LANG=en>). Dashed lines represent scaled
 837 energies of 10^{-5} and 10^{-4} .



838

839

840 **Figure S5.** Simulated waveforms of a regular earthquake that occurred in northern Hyuga-nada.

841 (a) Focal mechanism of the regular earthquake listed in the catalog by Takemura et al. (2020;

842 catalog: doi:10.5281/zenodo.3821172). Black line, inverted triangles, and dotted contours are the

843 same as displayed in Fig. 6. (b) Observed (black lines) and simulated (red lines) waveforms of

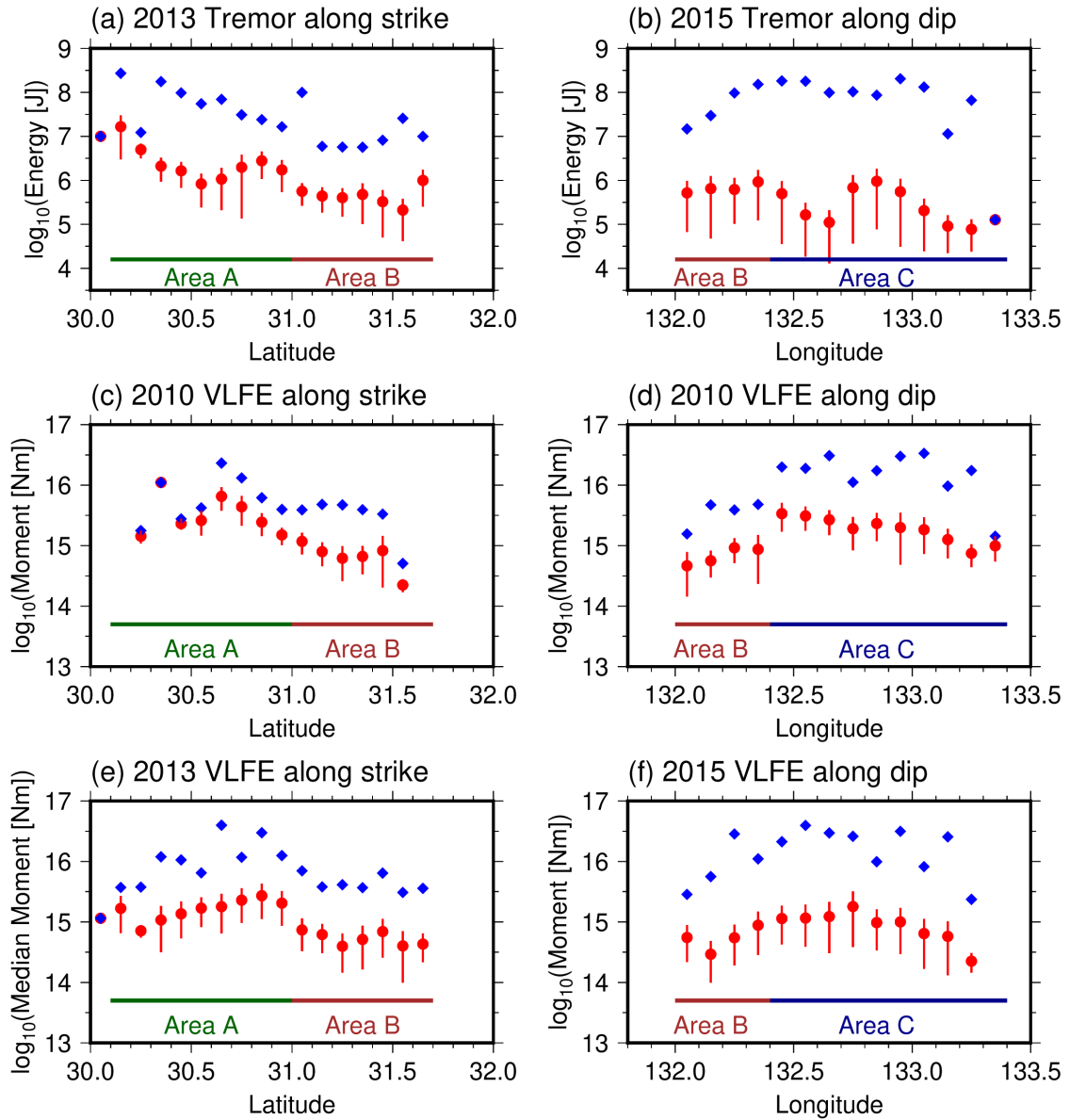
844 the earthquake at each F-net station. The assumed source time function was a Küpper wavelet

845 with a source duration of 1 s. Black and red lines are the observed and the simulated waveforms,

846 respectively. The simulation setting is the same as described in Section 2.2. R, T, and UB

847 components represent the radial, transverse, and vertical components, respectively.

848



849

850

851 **Figure S6.** Variation in maximum and median of tremor energies and VLFE moments along strike

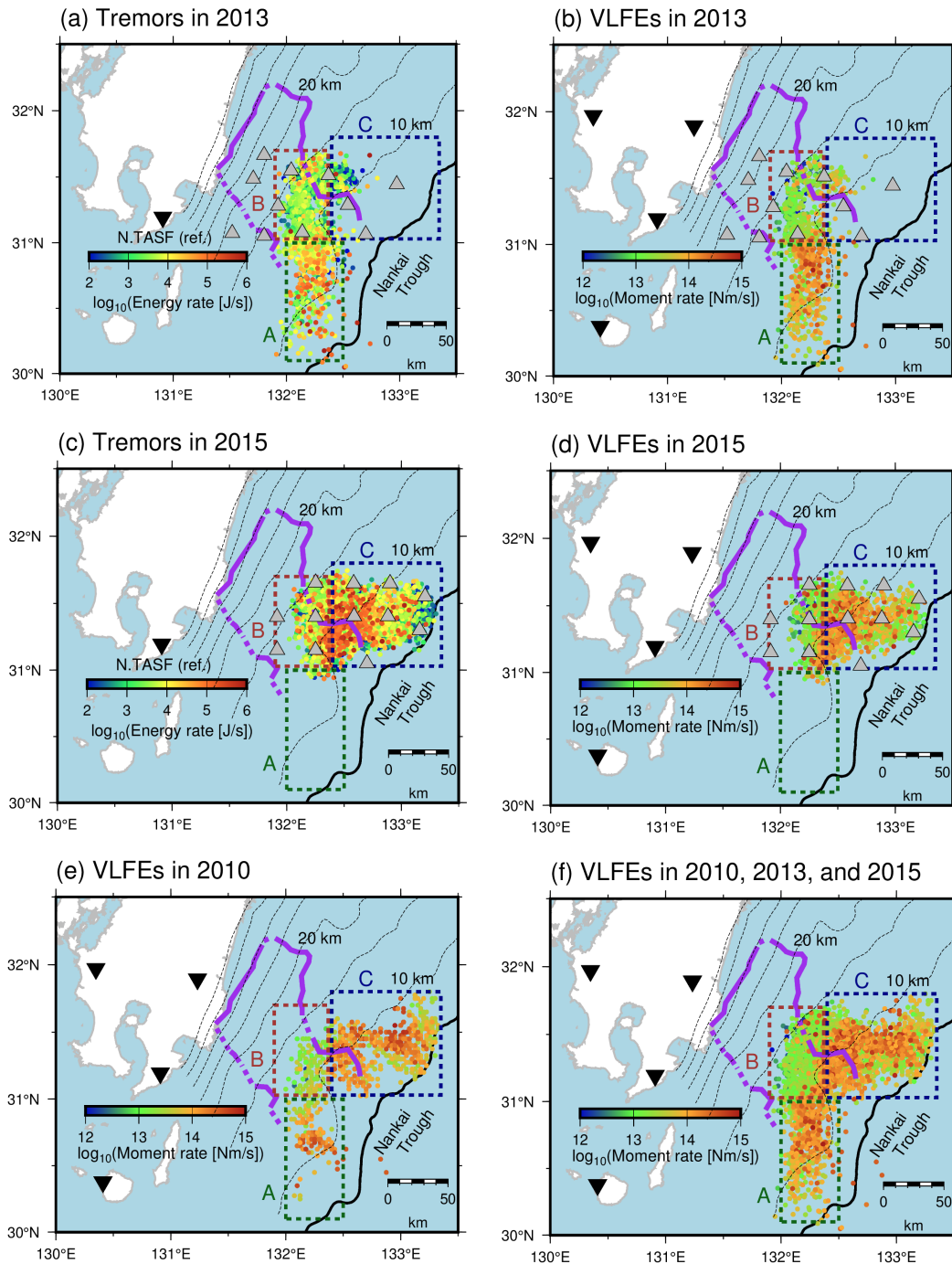
852 and dip directions at 0.1° interval. Blue diamonds and red circles represent the maximum and

853 median values, respectively. Red bars show the median absolute deviation of tremor energies and

854 VLFE moments.

855

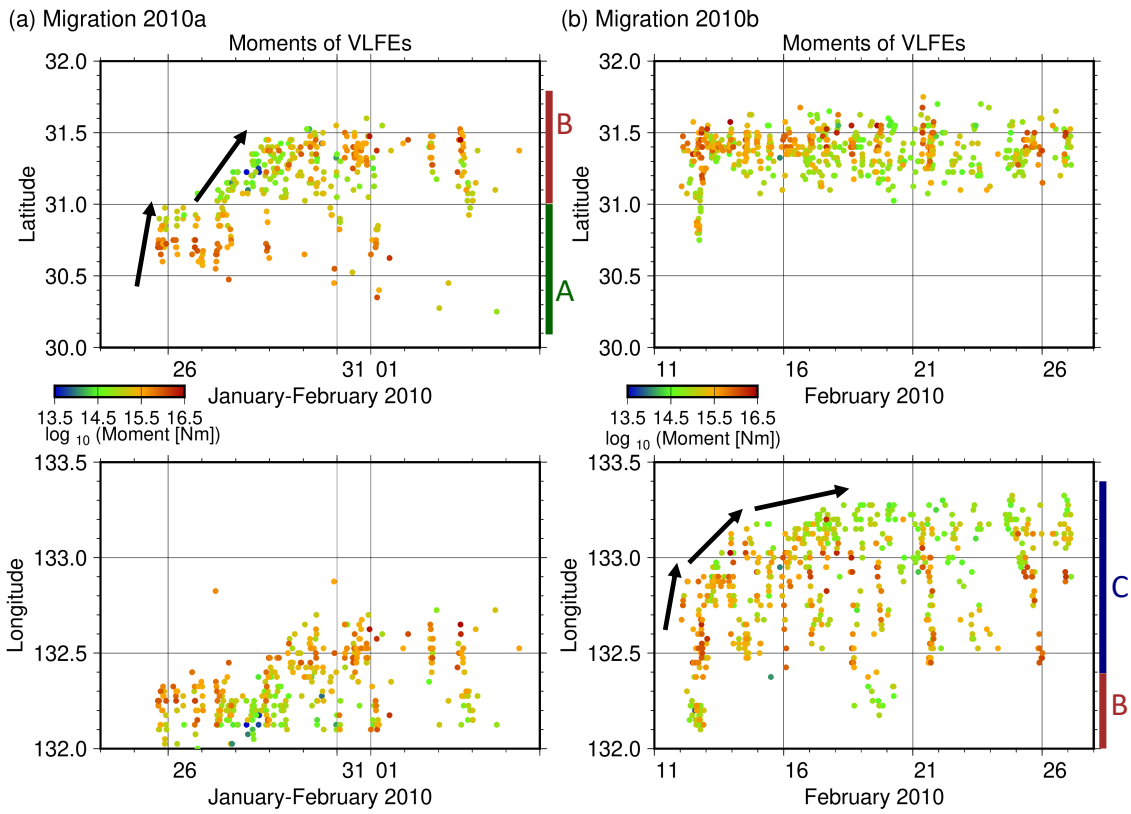
856



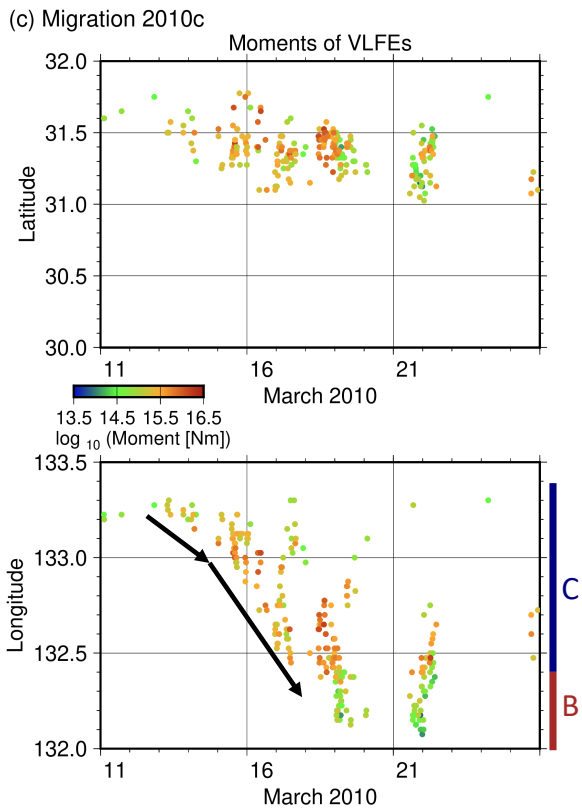
857

858

859 **Figure S7.** Spatial distribution of (a) energy rates of tremors in 2013, (b) moment rates of VLFs
 860 in 2013, (c) energy rates of tremors in 2015, (d) moment rates of VLFs in 2015, (e) moment
 861 rates of VLFs in 2010, and (f) moment rates of VLFs in all analysis periods. Colored dotted
 862 rectangles, dashed contours, purple lines, black line and gray triangles are the same as displayed
 863 in Fig. 7.

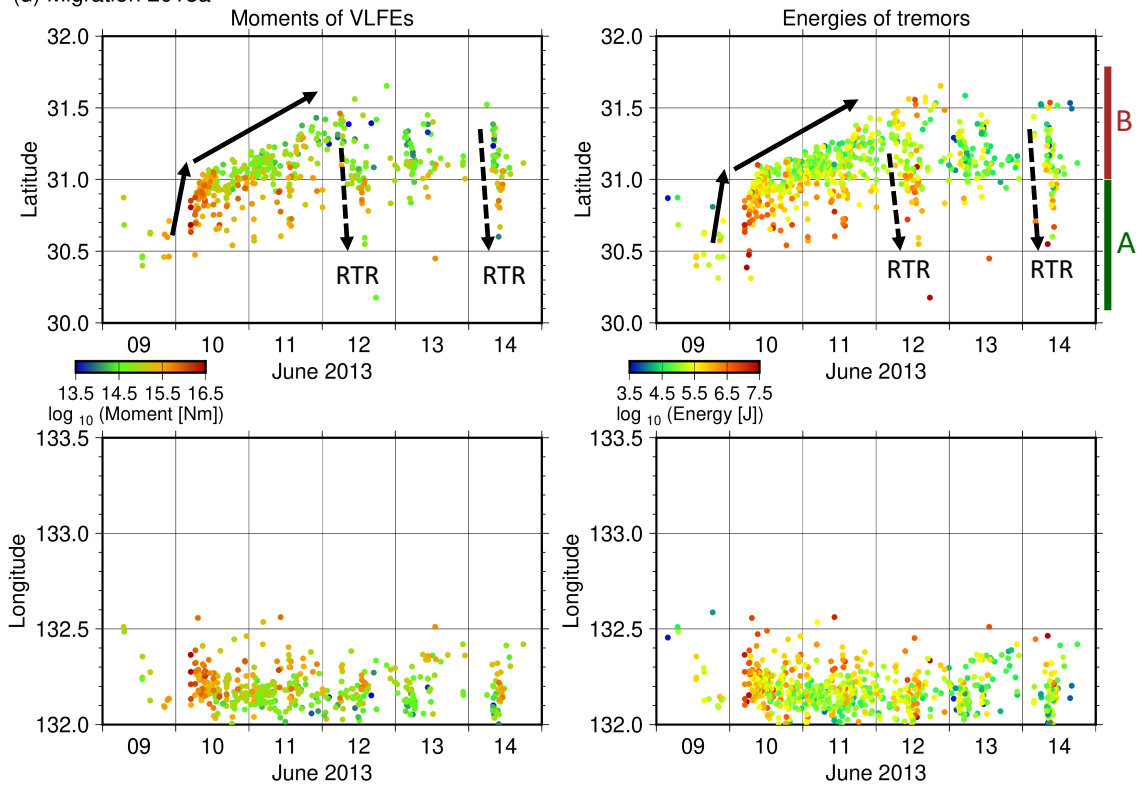


864



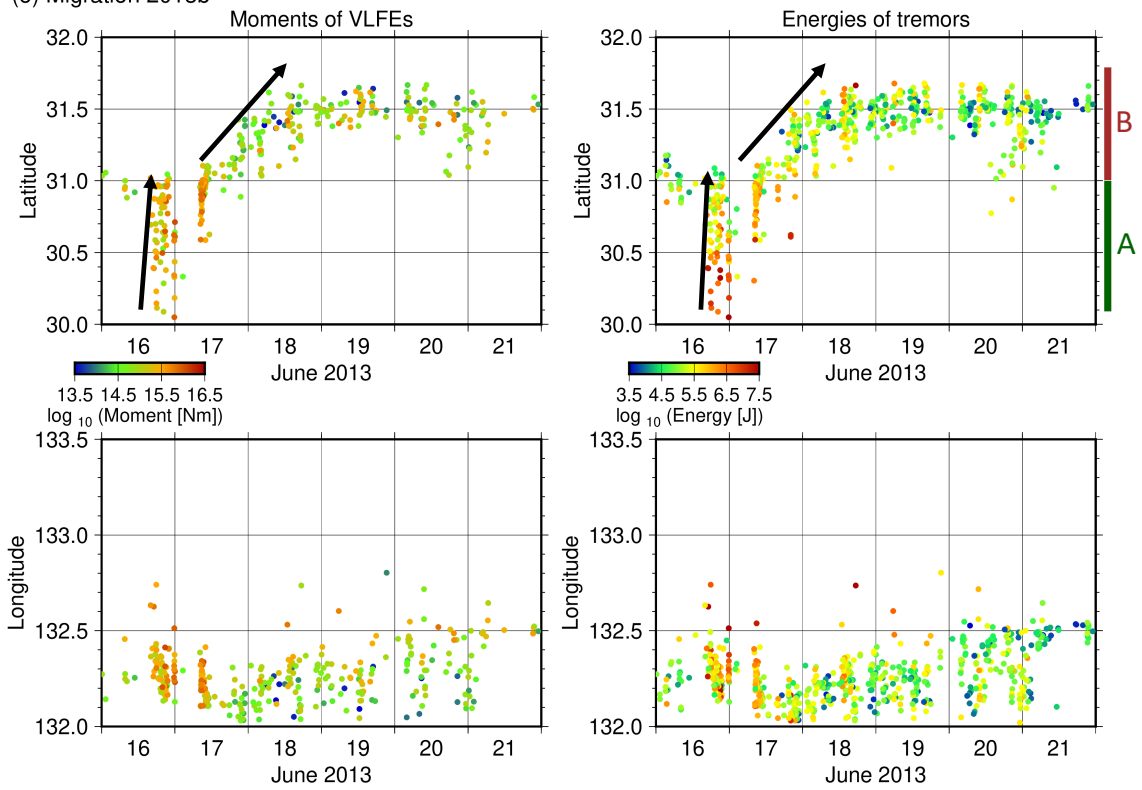
865

(d) Migration 2013a



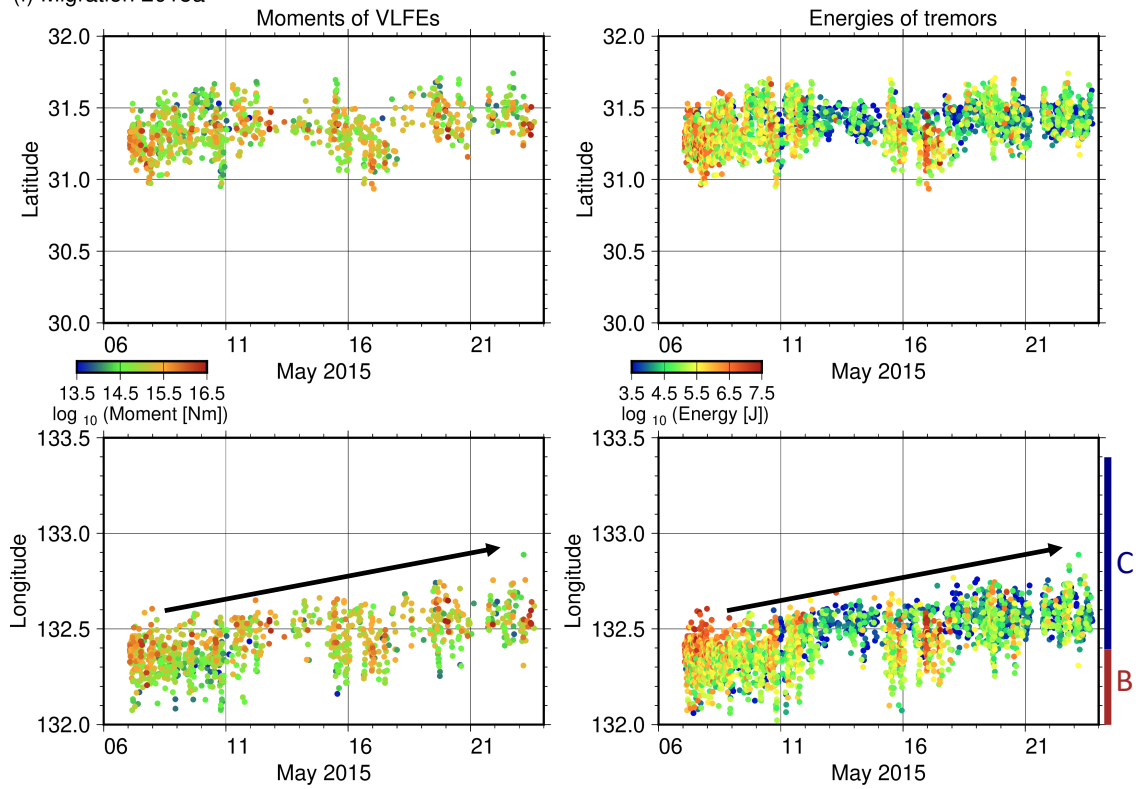
866

(e) Migration 2013b



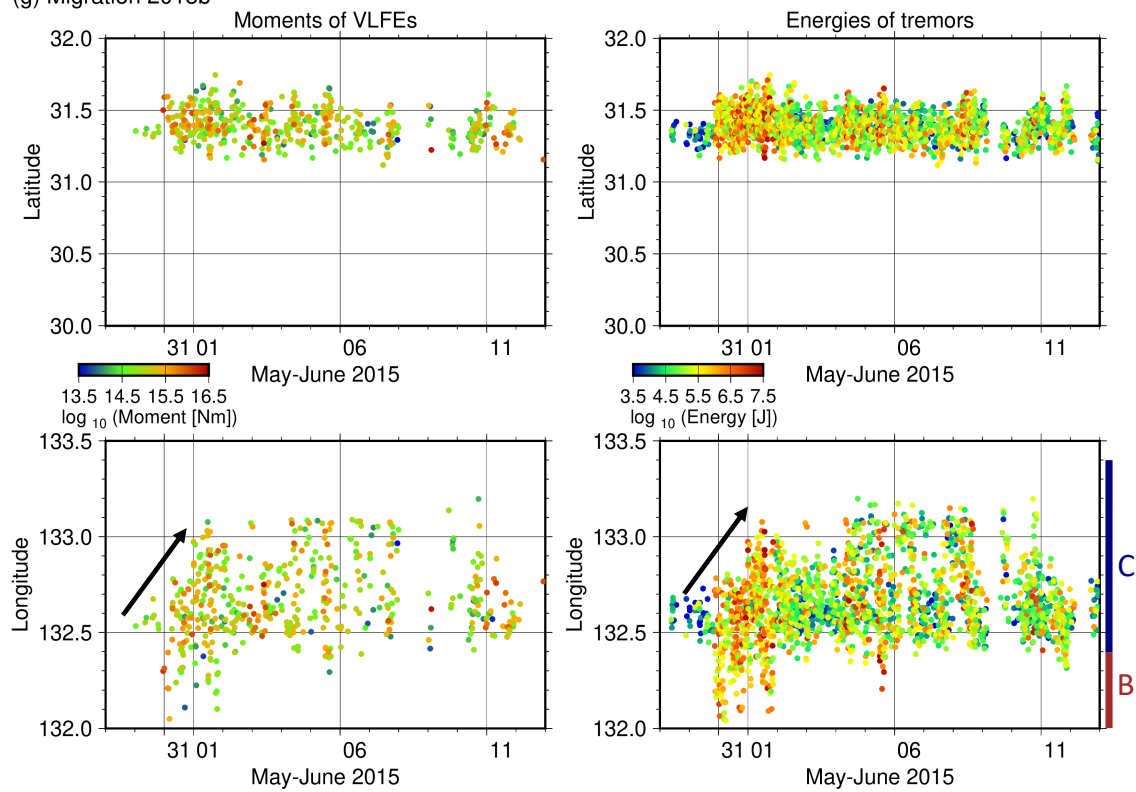
867

(f) Migration 2015a

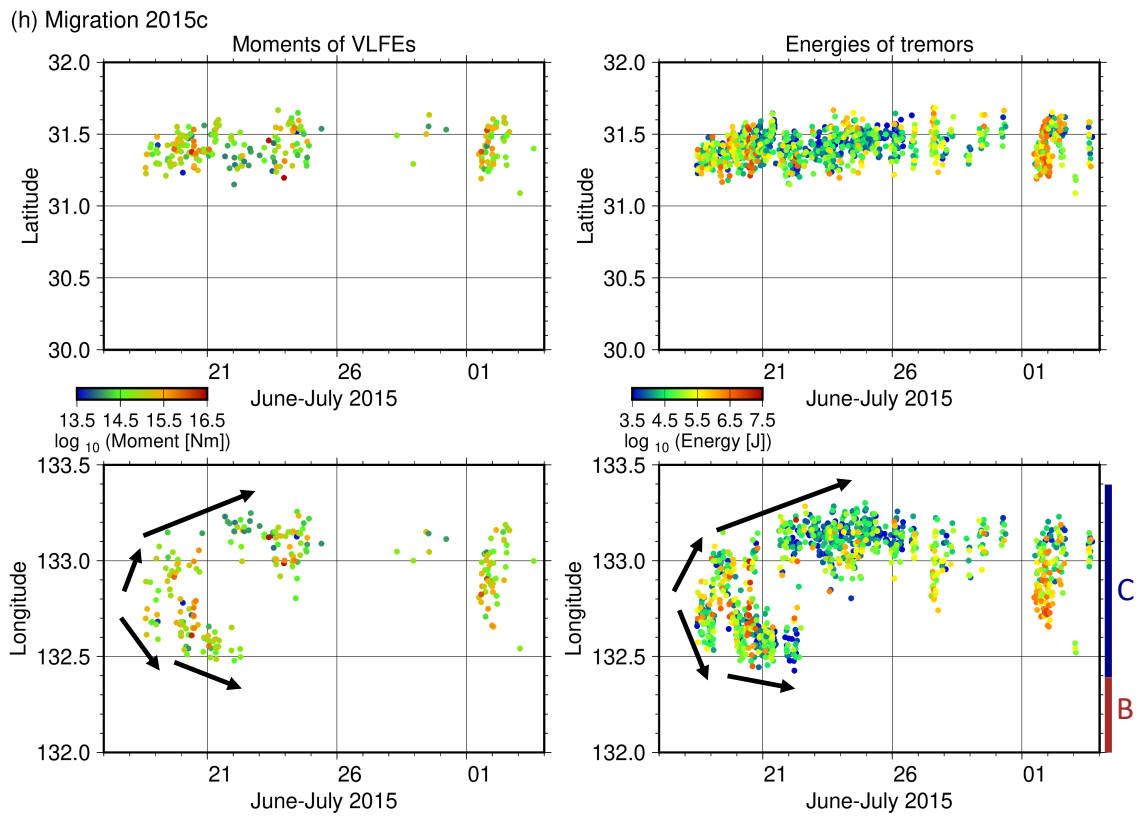


868

(g) Migration 2015b



869



870

871

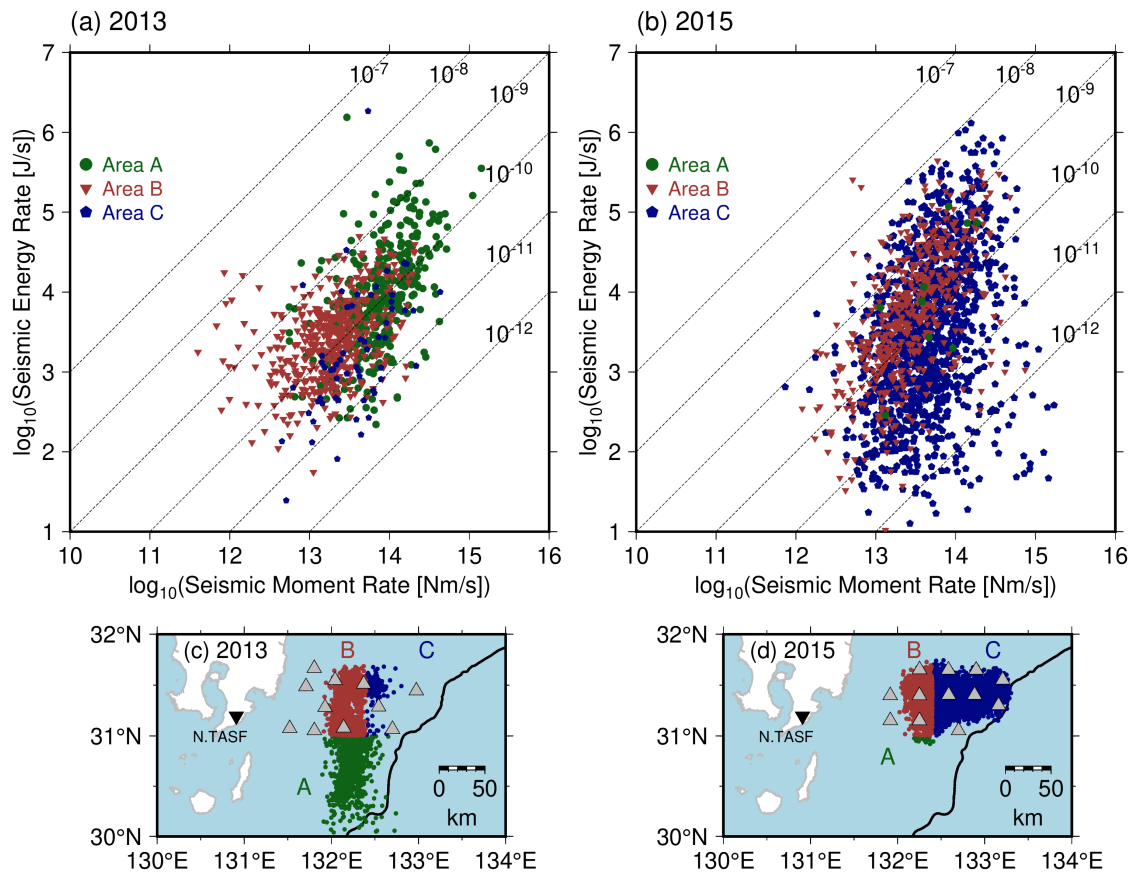
872 **Figure S8.** Spatiotemporal distributions of moments of VLFs and energies of tremors in the

873 directions along the N-S and E-W sections for each migration. Black arrows indicate the direction

874 of migrations. Black dotted arrows in Fig. S9d represents the rapid tremor reversal (RTR).

875

876



877

878

879

880

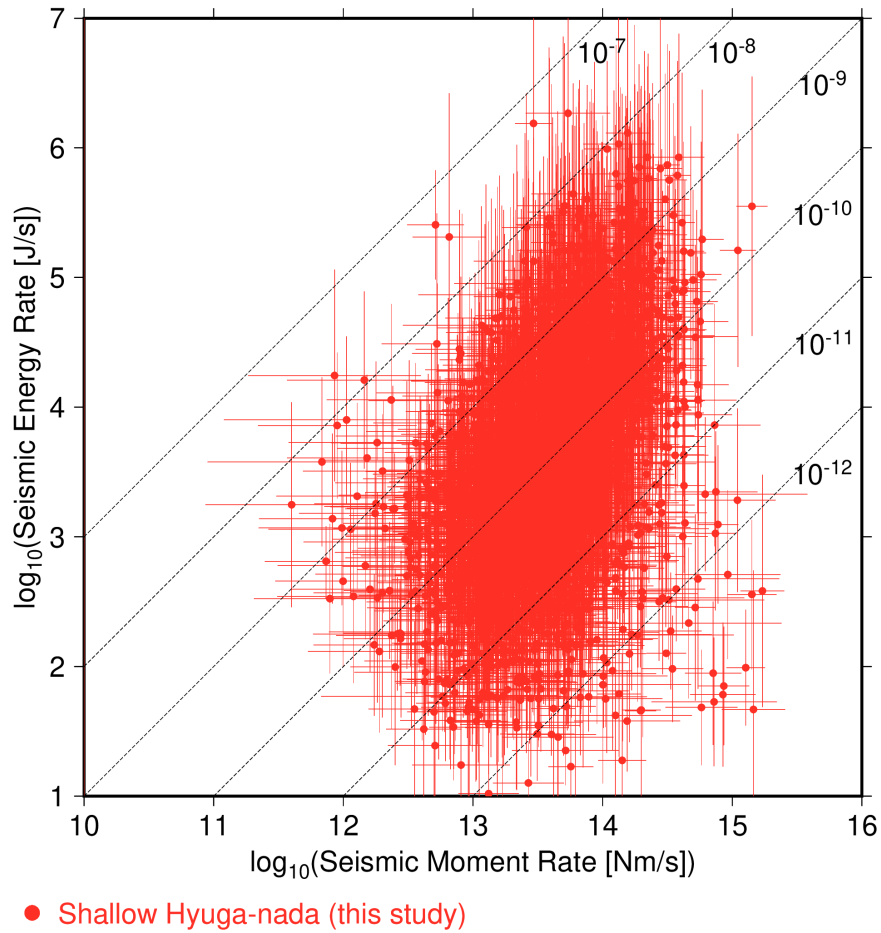
881

882

883

884

Figure S9. Relationship between seismic moment rates of VLFs and seismic energy rates of shallow tremors at each area in Hyuga-nada (a) in 2013 and (b) in 2015. Epicentres of shallow tremors at each area (c) in 2013 and (d) in 2015. Shallow tremors in Area A, B, and C are depicted by green, brown, and dark blue dots, respectively. Black lines, gray and black inverted triangles are the same as displayed in Fig.7.



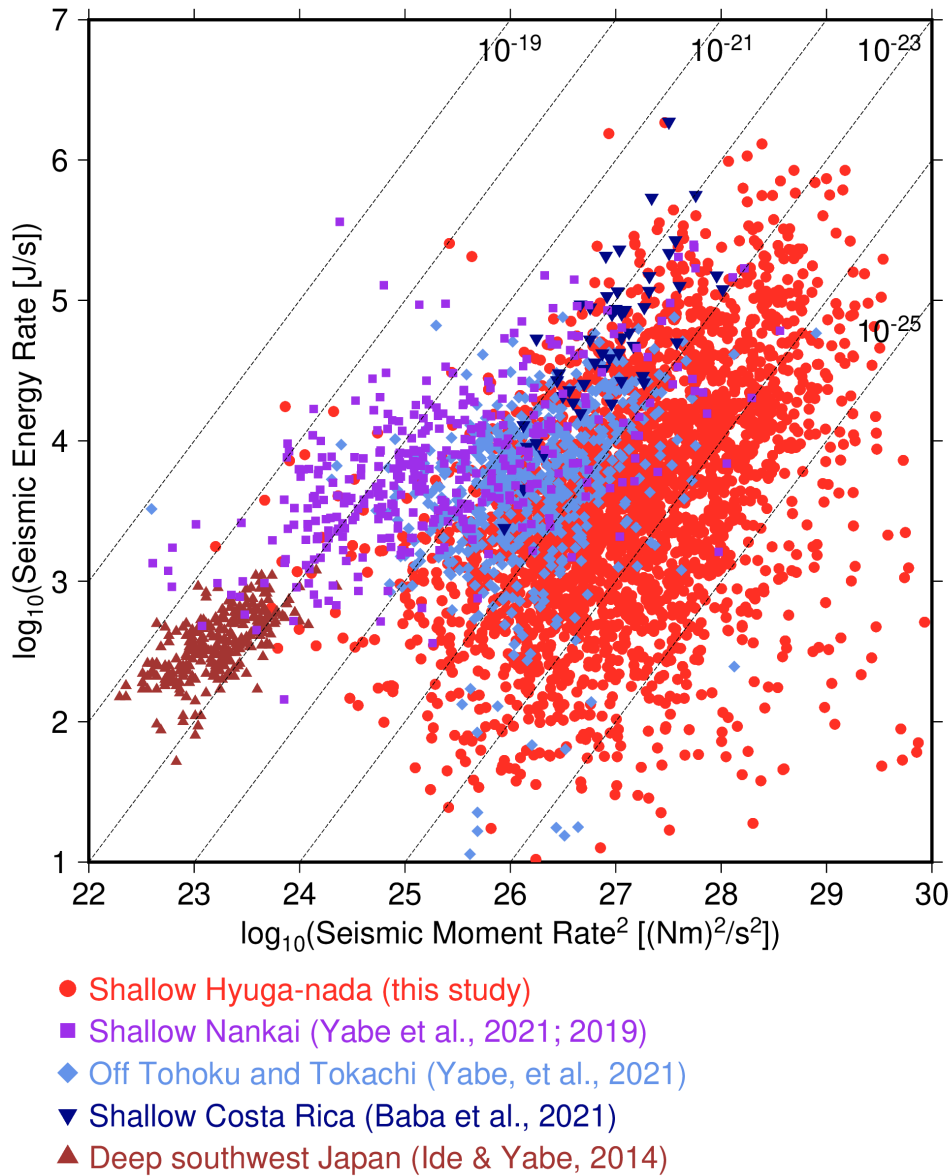
885

886

887 **Figure S10.** Relationship between seismic moment rates of VLFs and seismic energy rates of
888 shallow tremors with error bars in Hyuga-nada.

889

890



891
892
893
894
895
896
897
898
899

Figure S11. Relationship between seismic moment rates of VLFs and squared seismic moment rates of tremors. Red circles, purple squares, green diamonds, dark blue inverted triangles, and dark blue triangles indicate the relationships between seismic moment rates of VLFs and seismic moment rates of tremors in shallow Hyuga-nada (this study), shallow Nankai except Hyuga-nada (Yabe et al. 2021, 2019), off Tohoku and Tokachi (Yabe et al. 2021), shallow Costa Rica (Baba et al. 2021), and deep slow earthquakes (Ide, 2016; Ide and Maury, 2018; Ide and Yabe, 2014).

900 **Table S1.** Characteristics of migrations in Hyuga-nada.

901

Migration direction		
2010a	Along-strike	South to north
2010b	Along-dip	Downdip to updip
2010c	Along-dip	Updip to downdip
2013a	Along-strike	South to north
2013b	Along-strike	South to north
2015a	Along-dip	Downdip to updip
2015b	Along-dip	Downdip to updip
2015c	Along-dip	Bilateral

902

903